Development of non-blistering Si-rich layers for SiO_x-based passivating contacts using PECVD.

Relatore: Prof. Andrea LI BASSI

Tesi di Laurea di:
Alessandro ALLEVA   Matr. 919780

Contents

List of Figures

List of Tables

Abstract

With the increasing demand of high-efficiency solar photovoltaic devices, research has been focusing on strategies to increase the performance while cutting the production costs. In the silicon industry, one of the most promising technologies is represented by polycrystalline silicon passivated contacts. LPCVD is currently the main deposition technique used for the production of these contacts thanks to its high uniformity and coherence. On the other hand, LPCVD requires various additional steps because of the non-directional nature of it. PECVD represents a valid alternative thanks to the possibility of depositing on one side only and its availability in all the main solar cell production lines, although its use is challenging because of the frequent blistering of the deposited layers during the annealing step. Research has found that a suppression of blistering is possible when silicon is included with other elements such carbon, nitrogen or oxygen.

In this work, non-blistering C-, N- and O-incorporated silicon-rich layers were produced using PECVD. In addition, the post-annealing crystallinty and passivation quality of the so-obtained layers were measured. Blister-free layers were obtained starting from 1.6 $\dot{Q}_{CH_4/SiH_4}$, 0.26 $\dot{Q}_{NH_3/SiH_4}$ and 1.3 $\dot{Q}_{N_2O/SiH_4}$ flow ratios. A correlation between residual stress and blistering was also observed. The passivation quality of the PECVD layers was measured to be good, with values of J_0 as low as 1.3 fA/cm^2.

Estratto

La domanda per i dispositivi fotovoltaici ad alta effecienza è in aumento e la ricerca si è focalizzata in strategie per l'incremento delle prestazioni e il taglio dei costi. Nell'industria del silicio, una delle tecnologie più promettenti è rappresentata dai contatti passivanti a base di silicio policristallino. Attualmente la tecnica di deposizione più usata per la produzione di tali contatti è la LPCVD, grazie alla sua alta uniformità e coerenza. D'altra parte, essa richiede vari passaggi addizionali a causa della sua caratteristica non direzionalità. La PECVD rappresenta una valida alternativa grazie alla possibilità di deporre su un lato solo del dispositivo e alla sua grande disponibilità all'interno delle comuni linee di produzione di celle fotovoltaiche sebbene il suo utilizzo è insidioso a causa della frequente vescicolazione dello strato depositato. Una possibile soluzione alla vescicolazione è l'inclusione di carbonio, azoto o ossigeno nello strato di silicio da deporre.

In questo lavoro di tesi sono stati prodotti mediante PECVD vari strati privi di vescicole grazie all'aggiunta di carbonio, azoto e ossigeno. Successivamente sono state valutate la cristallinità post ricottura e la qualità di passivazione di questi strati. A partire da rapporti di flusso di $\dot{Q}_{CH_4/SiH_4}$, $0.26\ \dot{Q}_{NH_3/SiH_4}$ e $1.3\ \dot{Q}_{N_2O/SiH_4}$ sono stati ottenuti strati privi di vesciole ed è stata misurata una correlazione tra lo stress residuo e la propensione alla vesciolazione. La qualità di passivazione degli strati ottenuti mediante PECVD è stata misurata e ritenuta buona, con il più basso valore di J_0 ottenuto di $1.3\ fA/cm^2$.

Chapter 1

Introduction

In the last years, solar photovoltaic (PV) has reached a capacity of 500 GW which is believed to be followed by another 500 GW of installations within 2022-2023, establishing the beginning of the TW-scale PV era [6]. In 2019 the global energy need was of 20 TW (174000 TWh) [7] for which PV would account 5 % of the total demand. Among all the PV cell technologies, more than 95 % of the market share is represented by crystalline silicon (c-Si) technologies [1] which are in continuous development for performance enhancement and cost cutting. In the present days, c-Si cell research is focused on implementing the so-called "passivated" contacts or junctions which are technologies combining carrier selectivity with surface passivation, thus minimizing carrier recombination losses. The record efficiency of 26.7 % was reached in 2017 with silicon heterojunctions (SHJ) by Yoshikawa et al. [8] giving this approach a push forward in the global market share. Another passivated contact technology, which is the one that will be treated in this thesis, is based on doped polycrystalline silicon (poly-Si) junctions. These junctions are made by inserting a thin layer of silicon oxide (SiO_x) in between the silicon wafer and the highly doped poly-Si contact layer. It is common to refer to these contacts as tunnel oxide passivated contacts (TOPCon) or poly-Si/SiOx passivated junctions. With these contacts, devices with efficiency exceeding 26 % have been fabricated both with p- and n-type substrates and in different architectures (front- and back-contacted or interdigitated). In addition, the fabrication of these contacts requires processes which are already present in most of the industrial production lines [1]. For the above-mentioned reasons, research has been focusing on TOPCons and large-area production pilot lines already exist in two of the main solar cells manufactures.

1.1 Structure and working principle of poly-Si/SiO$_x$ contacts
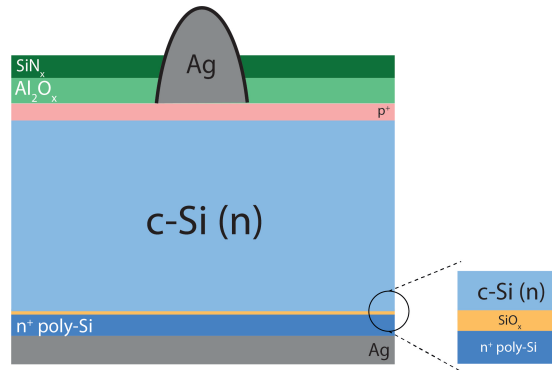
Figure 1.1: Diagram of a n-type solar cell featuring a rear phosphorous-diffused poly-Si/SiO$_x$ passivated junction. The picture is not in scale.

A typical TOPCon cell features a top boron-difused junction and a rear poly-Si/SiO$_x$ passivated junction, as shown in Fig. 1.1. The role of SiO$_x$ is crucial for the fabrication of such contacts as it acts as a dopant diffusion barrier. This way, the poly-Si layer is sharply separated from the absorber, thus minimizing recombination. Moreover, SiO$_x$ avoids epitaxial growth of the depositing silicon. Carrier selectivity is then obtained thanks to the heavily doped poly-Si layer, while surface recombination is reduced by the presence of the SiO$_x$ interfacial layer.

1.2 Motivation

As said previously, poly-Si/SiOx passivated junctions requires production technologies which are already present in most of the production lines and research facilities. An overview on the required steps is reported in Fig. 1.2

As it is possible to notice, the poly-Si layer deposition can be performed by means of physical vapor deposition (PVD) or chemical vapor deposition (CVD). In CVD, silane (SiH$_4$) is used as the precursor gas and the resulting deposit is either poly-Si or amorphous silicon (a-Si) which will crystallize during the high-temperature annealing step. Currently, low-pressure CVD (LPCVD) is the preferred method used in industry because of the high uniformity and consistence of results that is possible to achieve with this deposition technique. However, LPCVD, which is usually performed in low-pressure quartz tubes, is not directional and, thus, an extra etching step is required to remove the deposit from one of the sides of the silicon wafer. A possible solution for this problem is the adoption of plasma-enhanced CVD (PECVD) for the deposition step. This
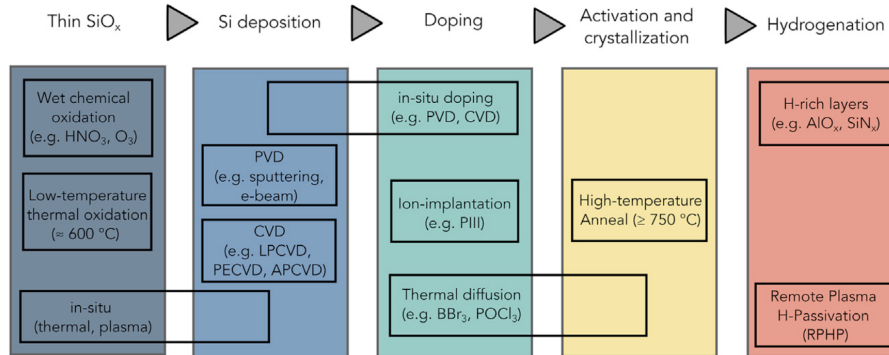
Figure 1.2: Production steps for TOPCons. The horizontal boxes indicates the different techniques that can be used to perform different steps [1].

technique can be used to deposit silicon on one side only and results of the same quality of LPCVD ones have been widely reported in literature [1]. In this case, the deposited layer is hydrogenated amorphous silicon (a-Si:H). Hydrogen will then be released during annealing, resulting in a poly-Si layer. The main drawback of this technique is the formation of blisters in the a-Si:H film during the deposition or, mainly, as a consequence of the annealing step, which is reported to be an effect related to the presence of hydrogen in the as-deposited a-Si:H layer [9], [10], [11]. A possible solution to this problem was proven to be alloying the amorphous silicon with carbon and very good quality contacts were obtained with silicon-rich silicon carbide layers [4], [12]. The reason behind the higher resistance to blister of this material is attributed to C-H bonds which are stronger than Si-H bonds [13], [14].

In this work, alloying will be the main strategy for the production of non-blistering PECVD layers. In addition to C-included layers, also N-included and O-included layers will be produced to evaluate blister suppression with inclusions of other types. The aim of this thesis will be the investigation of the blistering mechanism in PECVD a-Si:H layers, the production of non-blistering poly-Si layers using PECVD as the deposition step, and the performance assessment of those layers, with a comment on the possible implementation of the produced layers in devices. This work was conducted in Imec (Leuven) inside the PVC team, with the supervision of Rajiv Sharma and Prof. Jef Poortmans. All the cleaning and production steps were performed by me as well as the photoconductance and photoluminescence measurements and the imaging of the samples. Curvature measurements were performed by other operators as well as compositional analysis and raman spectroscopy. Data processing was performed by me.

11

1.3   Aim

The aim of this thesis is threefold:

1. Investigation of the blistering mechanism in PECVD a-Si:H layers,

2. The production of non-blistering PECVD Si layers by incorporating C, O, or N in the layer during PECVD, and

3. The performance assessment of those layers in relation to possible implementation in devices by means of lifetime measurements.

Chapter 2

Fundamentals

In this chapter, the fundamental mechanism of photoconversion and the theoretical basis to understand it will be discussed along with a section regarding the high efficiency strategies. All the information reported in this chapter is from the textbooks *Physics of solar cells* by Peter Würfel [15] and *The physics of solar cells* by Jenny Nelson [16] unless reported.

2.1 Semiconductors basics and solar cell working principle

Solar cells are devices capable of converting the absorbed radiation into electrical energy. The whole process consists of two main steps: the first one is the conversion of solar energy into chemical energy by absorbing photons while the second one is the transformation of the chemical energy into electrical energy by charge separation.

Considering an illuminated semiconductor as an example, for each photon with energy greater than the bandgap that is absorbed, an electron-hole pair (ehp) is created. The total chemical energy that is produced is then:

$$\eta_n + \eta_p = k_b T \ln\left(\frac{(p_0 + \Delta p)(n_0 + \Delta n)}{n_i^2}\right) \qquad (2.1)$$

Where n_i is the intrinsic carrier concentration, p_0 and n_0 are the equilibrium concentrations of holes and electrons respectively, and Δp and Δn are the excess carrier concentration that are generated by illumination, and since for each photon an ehp is created, $\Delta p = \Delta n$. The process consists of electron excitation to the conduction band and rapid relaxation (in the order of 10^{-12} s) to the band boundary, called in this case quasi Fermi level (QFL) as it is the actual fermi level but in a situation of non-equilibrium. If no driving force is applied, the pair will then recombine by emitting a photon or a sufficient number of phonons at one time. On the other hand, if a chemical potential gradient is

applied, charges can separate and diffuse to opposite terminals. To understand what is the nature of the driving force to be applied, it is firstly useful to recall the equations that describe charge currents in semiconductors in the one dimension case:

$$J_n = \mu_n n \frac{dE_{Fn}}{dx} = qD_n \frac{dn}{dx} - q\mu_n n \frac{d\phi}{dx} \tag{2.2}$$

$$J_p = \mu_p p \frac{dE_{Fp}}{dx} = -qD_p \frac{dp}{dx} - q\mu_p p \frac{d\phi}{dx} \tag{2.3}$$

E_{Fn} and E_{Fp} being the QFL of electrons and holes respectively and $d\phi$ the gradient of the potential of the charges. The electrons and hole mobilities are μ_n and μ_p, respectively, while D_n and D_p are the diffusivities.

From these equations, it is possible to conclude that the driving force is the gradient of the QFL that can be split into two contributions: one is the chemical potential gradient, while the other is the electrical potential gradient.

2.1.1   Doping

Doping of semiconductors is the process of inserting impurities in the crystal of the material. Usually, atoms are inserted as substitutional impurities in the lattice. It is then possible to classify dopant as donors or acceptors. Donors are the atoms which have one more valence electron compared to the ones of the semiconductor, while acceptors have one less valence electron.

When a donor atom is inserted in the lattice, the extra electron that remains unbounded is still interacting with the dopant by means of Coulombian attraction. The energy of this bond, though, is low because of the polarization due to all of the surrounding atoms. The extra electron can be then easily moved to its free state. For this reason, the new energy level introduced by this inclusion is slightly below the conduction band and hence the name donor is justified: a dopant which is a donor can promote its extra electron in the conduction band of the crystal with very low energy, being an electron donor for the conduction band. Being the introduced extra charge carrier an electron, semiconductors that have been doped with donors are called n-type semiconductors.

On the other hand, acceptors are atoms which leave one bond unfilled. Due to this reason, an electron can easily occupy the vacancy but it will not bind to the dopant and its interaction with the lattice is only ruled by the surrounding atoms. For this reason, a new level is added slightly above the valence band. The hole added in the lattice by the acceptor insert a positive charge carrier in the semiconductor and, for this reason, these materials are called p-type.

It is useful to introduce the equations which allow to calculate the quasi Fermi levels of the doped semiconductors:

$$E_{Fn} = E_c + k_b T \ln\left(\frac{N_D}{N_C}\right) \tag{2.4}$$

$$E_{Fp} = E_v + k_b T \ln\left(\frac{N_A}{N_V}\right) \tag{2.5}$$

14

Where N_D and N_A are the donor and acceptor concentrations and N_C and N_V are the effective densities of states of the conduction and the valence band respectively. E_c and E_v are the energies of the conduction and valence band in the undoped situation, k_b is the Boltzmann constant and T is the temperature.

2.1.2 Homojunction solar cells

Homojunction solar cells are characterized by a pn homojunction which is usually referred to as emitter. A pn homojunction can be obtained by diffusing a p-type dopant at one side of a n-type semiconductor. At the junction, due to the concentration gradient, electrons from the n-type semiconductor diffuse in the p-doped region while holes diffuse the opposite way. This process leaves the n-type region with an excess of positive ions and the p-type region with an excess of negative ions. An electric field is then established inside the junction which counters the concentration gradient, bringing back the system to the thermal equilibrium. Due to the absence of free carriers in the region, the zone around the junction is called depletion region. Fig. 2.1 schematize the situation.
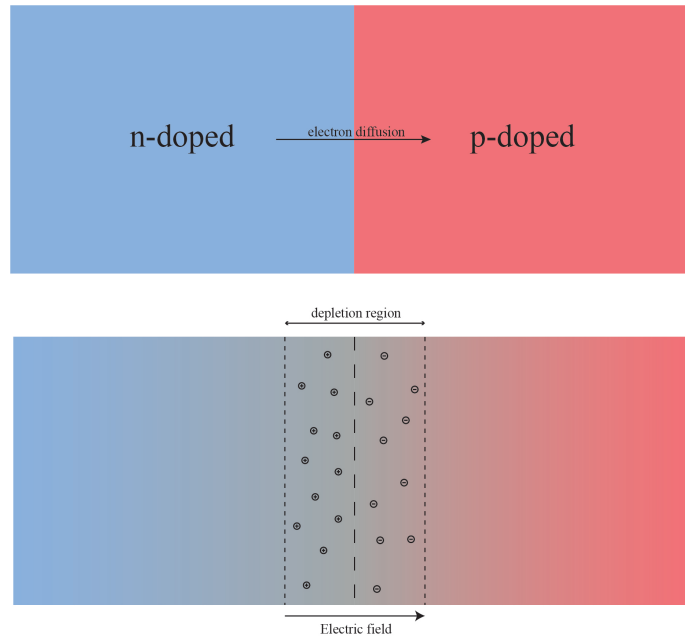
Figure 2.1: Electrons and holes first diffuse as a consequence of the concentration gradient, the second image shows the depletion region that forms.

Considering the two differently doped part as isolated, the QFL can be evaluated through Eq. 2.4 and 2.5 and it is shown in Fig. 2.2a. When the two parts are brought in contact, the system reaches the thermal equilibrium and the energy levels are shown in Fig. 2.2b. The bias which is reached at the

junction is called built-in potential or diffusion voltage and writes:

$$V_{bi} = \frac{k_B T}{q} \ln \left(\frac{N_A N_D}{n_i^2} \right) \tag{2.6}$$

While in the dark state (and so, in thermal equilibrium), the electric field balances the concentration gradient at the junction, and the Fermi Level is the same across the device. As a consequence of photon absorption (illumination) this level splits in two levels according to Eq. 2.7:

$$E_{Fn} - E_{Fp} = k_B T \ln \left(\frac{n_p p_p}{n_i^2} \right) \tag{2.7}$$

The difference in the two levels creates an electro-chemical potential gradient along the device which is the main driving force for the charge separation.

In actual devices, electrodes are contacted to the surfaces so as to collect the separated charge carriers and generate electrical power. Usually, majority carriers would recombine with diffused minority carriers at the surfaces, leaving no power available for collection, as the Fermi levels at the two terminals could eventually reach the same energy if the recombination velocity is sufficiently high. To minimize this behaviour, carrier-selective layers are used at the contacts. These act as membranes which selectively allow only holes or electron to reach the electrodes. The most simple carrier-selective layer is a heavily doped region, p^+ for holes and n^+ for electrons. Under the energy point of view, the effect of p^+ and n^+ regions is the pinning of the bands at the two terminals, as shown by Fig. 2.2c. The Fermi level is now different at the two terminals since recombination is, in part, suppressed.

To maximize power collection is then necessary to enhance contact selectivity; in the case of heavily doped regions this condition applies:

$$N_{A,p^+} N_{D,n^+} \geq n_p p_p \approx \Delta n (N_A + \Delta n) \tag{2.8}$$

Under this condition, the bias in the absorber is equal to the Fermi Levels splitting at the electrodes. The following writes:

$$V_{bi} \geq \frac{E_{Fn} - E_{Fp}}{q} \approx \frac{k_B T}{q} \ln \left(\frac{\Delta n (N_A + \Delta n)}{n_i^2} \right) \tag{2.9}$$

It is also possible to refer to the level splitting in the absorber as implied open circuit voltage (iV_{oc}).

Efficiency and limitations

From Shockley homojunction theory it is possible to derive the equation of the J-V characteristic curve of a solar cell:

$$J = J_0 \left[\exp \left(\frac{qV}{k_b T} \right) - 1 \right] - J_{sc} \tag{2.10}$$

16
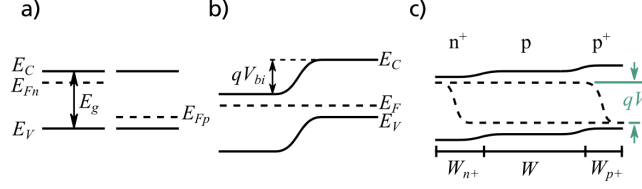
Figure 2.2: Fermi levels of a) n-doped and p-doped semiconductors alone, b) a pn homojunction in thermal equilibrium and c) an ideal $n^+|p|p^+$ device upon illumination.

Where J_0 is usually called reverse saturation current density and J_{sc} is the short circuit current density. According to Cuevas et al. [17], it is more correct to refer to J_0 as the recombination prefactor. From Eq. 2.10 it is possible to derive the expression for V_{oc} as follows:

$$V_{oc} = \frac{k_b T}{q} \ln \left(\frac{J_{sc}}{J_0} - 1 \right) \tag{2.11}$$

It is possible to notice that to obtain high values of V_{oc}, a very small recombination prefactor is needed.

The efficiency η is then evaluated by calculating the values of the fill factor (FF) that depends on J_{mpp} and V_{mpp} which are the values of J and V at the maximum power point (MPP):

$$FF = \frac{V_{mpp} J_{mpp}}{V_{oc} J_{sc}} \tag{2.12}$$

$$\eta = \frac{V_{oc} J_{sc} FF}{P_{in}} \tag{2.13}$$

η depends on V_{oc} which, in turn, depends on the recombination prefator J_0. As discussed by Feldmann in his PhD thesis [4], a model for J_0 in the case of homojunction solar cells exists and it shows that it is impossible to decrease J_0 indefinitely because the minority carrier recombination at the metal contact interface cannot be suppressed completely.

2.2 Strategies for high efficiency

In this section, an overview of some strategies for high efficiency will be provided. First, it is important to divide the approaches in two main groups, namely photon management, and carriers management. While the former group of strategies deals with the absorption phase of the device, the latter aims to develop architectures to reduce charge losses inside the device. Even if this work deals with a carrier management technology, a briefly introduction on the photon management techniques will be given for completeness.

2.2.1 Photon management

To obtain high-performance solar cells, it is first important to maximize the quantity of photons that the device is capable of absorbing. Especially for silicon, which is an indirect bandgap semiconductor, and so a bad photon absorber, light trapping is crucial to obtain an efficient device. Anti-reflective coatings are widely used to minimize reflectivity (that in the case of bare silicon is around 35 %). In this case, a thin-film (usually CVD SiN) is grown on top of the cell such that its optical thickness is equal to $\lambda/4$, where λ is the wavelenght of the incident light. This way, the light reflected by the SiN and the light reflected by the silicon surface interfere disruptively, thus minimizing reflection. As sunlight contains a whole spectra of wavelengths, in real cases also architectures which feature double or multiple coatings exist [2].

Additionaly, strategies to enhance the optical path of light inside the active material are used. The most simple one is the addition of a reflective layer at the rear side of the cell (Fig. 2.3b). This way the optical path becomes double with respect to the one of the bare wafer. It is also possible to texture the top surface with pyramidal features: the tilted facets are more likely to reflect the incident light which is not absorbed back to another pyramid, increasing the number of absorbed photons (Fig. 2.3c). Lastly, structures based on fully randomized texturing are being studied. In this case, the surface works by scattering the light preferably into the absorber, as its structure allows a denser phase space for light that the one offered by air (Fig. 2.3d) [2].
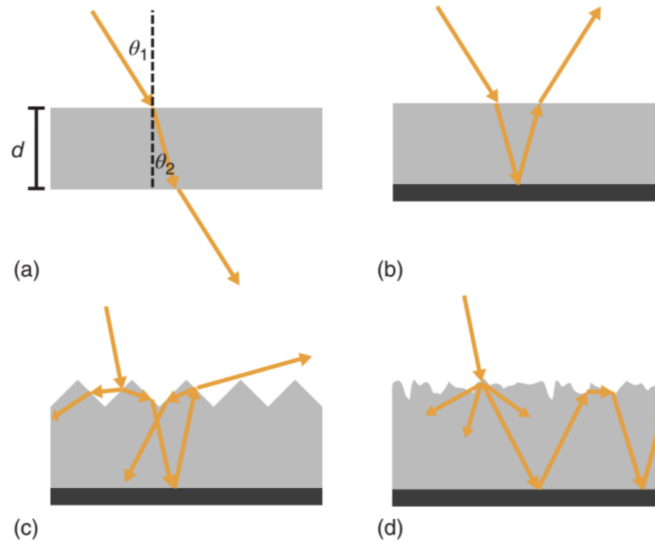
Figure 2.3: Optical path of light in the active layer in the case of a) bare wafer b) wafer with a reflector at its back surface c) pyramidal texture d) random scattering texture [2]

2.2.2 Carrier management

The other way of improving solar cells efficiency is to manage charge carriers. It is indeed important to avoid charge recombination such to be able to ideally extract all the carriers generated in the active material.

In general, it is possible to divide recombination mechanisms into two main groups: the unavoidable recombination mechanisms, which are the radiative recombination and the Auger recombination, and the avoidable recombination mechanisms, which are triggered by localized trap states which interact with charge carriers.

The spontaneous emission of a photon is the dominant radiative recombination in the case of solar cells, the other being the stimulated emission of photons, which is never occurring in such devices. The other unavoidable process is the Auger recombination, which is a process of scattering between similar charges. Auger recombination is of high importance when the bandgap is low and the carrier density is high, in which case, carrier-carrier interactions are very strong.

In the case of real semiconductors, the most important recombination mechanisms are the avoidable ones, also called non-radiative recombinations. These derive from the presence of defects in the material, which add available levels to the bandgap. When a carrier is trapped in the impurity level, it can be released by thermal activation or recombine if a charge of the opposite polarity is also trapped in the defect level. The name of these additional levels is trap-states if they lay close to the conduction or valence band, while they are usually called recombination centers if their energy is close to the center of the bandgap. The theory of non-radiative recombination has been developed by Shockley, Read and Hall, and the SRH recombination rate reads:

$$U_{SRH} = \frac{np - n_i^2}{\tau_{n,SRH}(p + p_t)\tau_{p,SRH}(n + n_t)} \tag{2.14}$$

Where $\tau_{n,SRH}$ and $\tau_{p,SRH}$ are the average lifetimes for electron and hole capture, respectively, and n_t and p_t are the density of electrons and holes when their Fermi energy is equal to the trap level energy.

In a solar cell, electrons and holes recombine either in the bulk of the active material or at its surfaces. The rate in Eq. 2.14 is maximized when the density of carriers (n for electrons and p for holes) is of the same order of magnitude, so in undoped regions SRH recombination will be predominant. Also, as $\tau_{n,SRH}$ and $\tau_{p,SRH}$ are quantity inversely proportional to the trap state density, SRH recombination will be present in highly defective areas such as grain boundaries and surfaces.

Recombination in the bulk depend on the c-Si defect density and doping level. As the wafer type will be a fixed parameter for all the experiments performed in this thesis, strategies to improve bulk lifetimes will not be discussed. On the other hand, recombination at the surfaces is of high interest for this work. The main scope of contacts for high-efficiency solar cells is to limit carrier recombination at the contacts as to enhance energy collection.

2.2.3 poly-Si/SiO$_x$/c-Si contacts
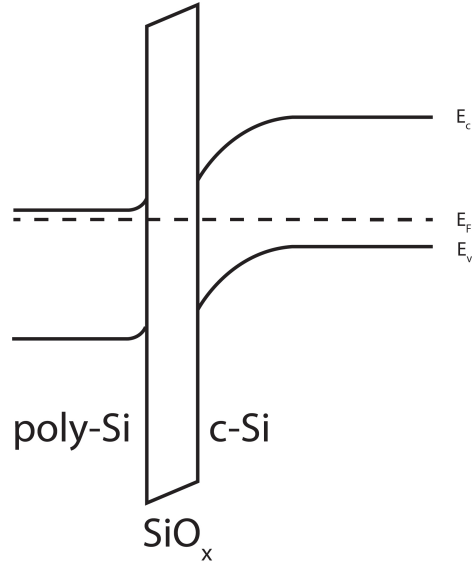
Figure 2.4: Band structure of a (n)poly-Si/SiO$_x$/c-Si contact.

The poly-Si/SiO$_x$/c-Si band structure is reported in Fig. 2.4. As it is possible to observe, the SiO$_x$ layer creates a potential barrier which allows charge current by means of tunneling of carriers. In the case of a n$^+$ poly-Si contact, the hole tunneling probability can be calculated with the WKB approximation as [4]:

$$T_n \approx \exp\left(-\frac{2\delta}{\hbar}\sqrt{2m_h^* q \Delta\phi_h}\right) \tag{2.15}$$

In which δ is the barrier thickness and $\Delta\phi_h$ is the barrier height for holes. The same apply for p$^+$ poly-Si contacts, with $\Delta\phi_n$ being the barrier height for electrons. By suitably doping the poly-Si layer, it is possible to shift the Fermi energy of it, so as to increase the potential barrier for one type of carriers and decrease the one for the other type, obtaining contact selectivity.

The role of poly-Si

The role of poly-Si in TOPCon is very important as it contributes to passivation and carrier-selectivity in three ways [18]:

1. As introduced previously, poly-Si produce a field effect which can be more or less evident depending on the concentration of dopants. The tunneling current can be then easily controlled by controlling the concentration of dopants.

2. In the case of p-doped poly-Si, dopants produce also a gettering effect at the c-Si surface as studied by Liu et al. [19]. Poly-Si is then important to improve bulk quality of the wafer as gettering is defined as the confinement of impurities from the active region in predetermined passive region of the wafer [20].

3. It also acts as a barrier in the metallization step, by avoiding SiO_x rupture due to metal contact fabrication.

Chapter 3

Characterization techniques

In this chapter, a theroetical background and a description of all the techniques used to collect, process and interpret data is reported.

3.1 Carrier lifetime

To be able to compare different contact layers, the measurement of the carrier lifetime is a crucial step.

The minority carrier lifetime is the average time spent by a charge carrier before recombination with its opposite type [21]. After generation in the semiconductor, charges occasionally recombine before being extracted at the terminals. In order to enhance the electrical energy collection, this mechanism needs to be suppressed and this section will explain all the techniques that allow to analyze this phenomenon.

3.1.1 Generation and recombination

Letting G_L be the generation rate, that is the rate at which the excess of carriers Δn (or Δp, as the amount of positive carrier is assumed identical to the amount of negative ones) is generated by illumination in a unit volume, $R = \frac{\Delta n}{\tau}$ be the recombination rate with τ representing the average carriers lifetime, the following equation holds if no net current is flowing in the control volume:

$$G_L - \frac{\Delta n}{\tau} = \frac{d\Delta n}{dt} \qquad (3.1)$$

Which simply tells that the rate of change of the excess carriers in time is the difference between the generation and the recombination rates.

It is possible to further deepen this equation by writing G_L in function of measurable parameters. With Φ_{ph} being the flux of the photons with energy higher than the material bandgap, and considering that all the absorbed photons

lead to exciton formation uniformly across the wafer thickness, G_L writes:

$$G_L = \frac{(1 - R)\Phi_{ph}}{W} \qquad (3.2)$$

Where the term $(1 - R)$ accounts for the loss due to reflection of the incident photon flux, R being the reflectance of the sample and W its thickness.

Combining Eq. 3.1 and Eq. 3.2 it is possible to obtain:

$$\frac{(1 - R)\Phi_{ph}}{W} - \frac{\Delta n}{\tau} = \frac{d\Delta n}{dt} \qquad (3.3)$$

R and Φ_{ph} being easily measurable quantities, only $\frac{d\Delta n}{dt}$ is needed to be able to evaluate τ.

3.1.2 Photoconductance

As discussed before, upon illumination an excess of charge carriers is generated and being able to measure this quantity is crucial for lifetime measurements. The simplest and most widely diffused way to do this is to measure the change of conductance of an illuminated sample [21]. Such a measure can be performed either by inserting the wafer in a circuit and measuring the change in voltage drop or, in an easier way, placing it on the top of an inductor which, in turn, is part of an RF circuit.

The conductivity increase due to an excess of carrier is:

$$\Delta\sigma = qW(\mu_n + \mu_p)\Delta n \qquad (3.4)$$

Where W is the wafer thickness and μ_n and μ_p are, respectively, the electrons and the holes mobility.

3.1.3 Steady state and transient decay

In real conditions there are two ways of performing lifetime measurements. The first is called steady state regime and it applies when the rate of generation is perfectly balanced by the rate of recombination. Mathematically, $\frac{d\Delta n}{dt} = 0$ and Eq. 3.3 becomes:

$$\frac{(1 - R)\Phi_{ph}}{W} = \frac{\Delta n}{\tau} \qquad (3.5)$$

The average lifetime is then easily evaluated by inverting the formula. The main disadvantage of performing a measurement in this regime is that the measurement that is obtained is relative only to a specific level of injection Δn.

The other regime called transient decay (it is also possible to refer to it by means of photoconductance decay, from now on PCD) applies when, after an excess of carriers has been injected (that is, $\Delta n \neq 0$), generation stops abruptly. In this case, Eq. 3.2 reads:

$$-\frac{\Delta n}{\tau} = \frac{d\Delta n}{dt} \qquad (3.6)$$

PCD overcomes the disadvantage of SSPC (steady state photoconductance) by means of being able to measure τ for a wide range of injection levels with a single investigation.

However, for silicon wafers in which lifetimes are shorter than 50 μs, two effects (namely surface recombination transient and minority carrier spreading) are present and, because of this, the interpretation and application of this type of measurement is complicated [22].

3.1.4 Quasi steady state photonductance

It is possible to combine the two techniques described before to exploit the advantages of both in the so called: "Quasi steady state" photoconductance (QSSPC), firstly proposed by Sinton et al. in 1996 [22][21]. The experimental condition used in QSSPC is the usage of a light source that varies in time in a way which is slow compared to the lifetime of carriers in the wafer. In the QSS regime, recombination, generation and carrier density change are physical phenomena present at the same time.

To find the mathematical relation that describes this regime, it is useful to define a net photogeneration rate at a first place:

$$\Phi_{ph}(1-R)|_{net} = \Phi_{ph}(1-R) - W\frac{d\Delta n}{dt} \tag{3.7}$$

Introducing this expression in Eq. 3.5 in substitution of the generation rate proper of a steady state regime, it is possible to obtain:

$$\Phi_{ph}(1-R) - W\frac{d\Delta n}{dt} = \frac{\Delta nW}{\tau_{QSSPC}} \tag{3.8}$$

In this case, the carrier density is assumed uniform within the wafer thickness, this explains the term ΔnW. From Eq. 3.8 it is finally possible to find τ_{QSSPC}:

$$\tau_{QSSPC} = \frac{\Delta nW}{\Phi_{ph}(1-R) - W\frac{d\Delta n}{dt}} \tag{3.9}$$

QSSPC measurement is a complete approach that is capable of describing with very good approximation the lifetime of carriers within a semiconductor such as silicon. The quantity τ_{QSSPC} is the same lifetime which is measured with the two methods previously described. All of them describe the average time a charge carrier spends before recombination, independently from which mechanism is responsible for the recombination. That is the reason why it is common to refer to τ and τ_{QSSPC} as τ_{eff} (effective lifetime).

3.1.5 Surface recombination velocity

As said previously, carriers recombine by means of multiple mechanisms. In passivating layers technologies it is easy to understand that the main interest

relies on the effect that these surfaces have on carriers lifetime. In this scope it is convenient to first write the following relation:

$$\Phi_{ph}(1-R)|_{net} = \frac{\Delta n W}{\tau_{bulk}} + 2S\Delta n \tag{3.10}$$

Which is valid under the assumption of absence of surface potential. This equation points out that, in the QSS regime, the net photogeneration rate is balanced by the total recombination rate which, in turn, can be split in two different recombination mechanisms contributions: the first is relative to recombination in the bulk and its characteristic lifetime is represented by τ_{bulk}, while the second refers to recombination occurring at the surfaces, with S representing the surface recombination velocity (SRV). A well-passivated surface should express very low values of SRV.

Dividing Eq. 3.10 by $W\Delta n$ and combining it with Eq. 3.9 the following relation is obtained:

$$\frac{1}{\tau_{eff}} = \frac{1}{\tau_{bulk}} + 2\frac{S}{W} \tag{3.11}$$

Being able to evaluate τ_{bulk} is crucial for the determination of SRV. First, it is important to determine the different recombination mechanism occurring in the bulk which are: radiative recombination, Auger recombination and Shockley-Read-Hall (SRH) recombination. The average lifetime in the bulk is then:

$$\frac{1}{\tau_{bulk}} = \frac{1}{\tau_{rad}} + \frac{1}{\tau_{Aug}} + \frac{1}{\tau_{SRH}} \tag{3.12}$$

It is then useful to define the intrinsic lifetime τ_{intr} as:

$$\frac{1}{\tau_{intr}} = \frac{1}{\tau_{rad}} + \frac{1}{\tau_{Aug}} \tag{3.13}$$

Which can be calculated using the parametrization proposed by Richter et al. [23] knowing the dopant concentration and the temperature. The last parameter to be determined is the lifetime relative to the SRH recombination. This mechanism strongly depends on carrier injection rate but it is assumed to be negligible for high levels of injection [24].

3.1.6   Emitter saturation current density

Surface recombination velocity is a useful parameter for comparing different passivating layers. When a heavily doped emitter (or a diffused layer) is also present, recombination in its bulk and at its surfaces is usually predominant with respect to the recombination in the passivated layers underneath. A useful parameter to evaluate the quality of such emitters is the emitter saturation current density pre-factor J_0. This quantity has the physical meaning of a factor that multiplied with the normalized pn product gives the total recombination

current density in the zone of interest [25]. The proposed model to evaluate J_0 is similar to the one used to calculate SRV:

$$\frac{1}{\tau_{eff}} - \frac{1}{\tau_{intr}} = \frac{1}{\tau_{SRH}} + \frac{2J_0(N_{dop} + \Delta n)}{qn_i^2 W} \tag{3.14}$$

Where N_{dop} is the dopant concentration, n_i is the intrinsic carrier concentration and q is the unit charge of an electron [3]. It is sufficient to plot the curve $\frac{1}{\tau_{eff}} - \frac{1}{\tau_{intr}}$ versus the minority carrier injection Δn to find J_0 as the slope of the resulting curve as shown in Fig. 3.1. It is also possible to notice that $\frac{1}{\tau_{SRH}}$ is contained in the value of the intercept of the curve, along with a factor depending on J_0. For a good emitter, J_0 values of a few fA/cm^2 are expected.

As shown by Kale et al. [3], in some cases the resulting slope is flat, leading to a misinterpretation of the real value of J_0 as it is possible to notice in Fig. 3.1. In cases such as the one described, recombination is governed by the passivation layer and the value of SRV is preferred to evaluate the sample.
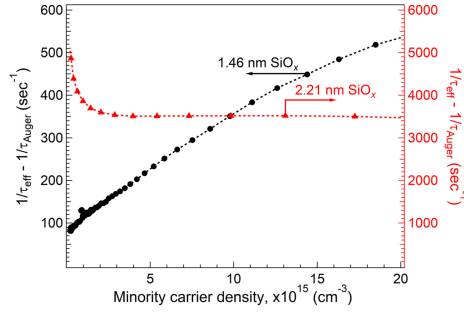
Figure 3.1: For well-passivated samples, non-zero slope is found, for badly passivated ones, SRV is predominant over J0 [3].

3.1.7 Injection rates

To conclude, it is useful to define what is intended for low and high injection rates. High injection rate is defined when $\Delta n \gg N_{dop}$. In this case Eq. 3.14 writes:

$$\frac{1}{\tau_{eff}} - \frac{1}{\tau_{intr}} = \frac{1}{\tau_{SRH}} + \frac{2J_0\Delta n}{qn_i^2 W} \tag{3.15}$$

In this case, the emitter contribution is predominant with respect to the one of the bulk and it is possible to assume that the effective lifetime is just inversely proportional to the emitter recombination current.

Low level of injection, on the other hand, is considered when $\Delta n \ll N_{dop}$. In this case the relation becomes:

$$\frac{1}{\tau_{eff}} - \frac{1}{\tau_{intr}} = \frac{1}{\tau_{SRH}} + \frac{2J_0 N_{dop}}{qn_i^2 W} \tag{3.16}$$

Low injection rate is useful to evaluate τ_{bulk} when using an emitter with a known very low J_0 value.

3.2   Raman spectroscopy

Raman spectroscopy is a technique that is based on the interaction of light with atoms. It is widely used for structural analysis of molecules as well as crystalline fraction evaluation of mixed phases. This characterization method is based on the Raman effect, which can be observed in molecules interacting with light that experience a change in the polarizability after the absorption of a photon.

When a molecule absorbs a photon, it is excited to a higher virtual vibrational state from which it relaxes resulting in the emission of a new photon. The energy of the emitted photon corresponds to the difference between the virtual vibrational level and the level occupied by the molecule after relaxation.

$$E_{ph} = \epsilon_v - \epsilon_i \tag{3.17}$$

In the case of relaxation to the original ground state ϵ_i that the molecule occupied before excitation, the energy of the emitted photon is the same of the energy of the absorbed one. This transition is called elastic scattering or Rayleigh scattering and it is the most frequent mechanism. On the other hand, Raman scattering refers to inelastic scattering which occurs when the emitted photon corresponds to the relaxation to a level higher or lower than the original one. In the case of emission of a photon with lower energy (relaxation to a higher level) the scattering is defined as Stokes scattering, while in the case of emission of photon with higher energy (relaxation to a lower level) the process is called anti-Stokes scattering. As this latter mechanism requires a molecule to be already excited to at least its first vibrational state, it is the less probable one. Fig. 3.2 is a summary of the three different scattering processes.

If a monochromatic light source is used, the Stokes shift is symmetrical to the anti-Stokes shift with respect to the energy of the Rayleigh scattering (that corresponds to the energy of the absorbed photons).
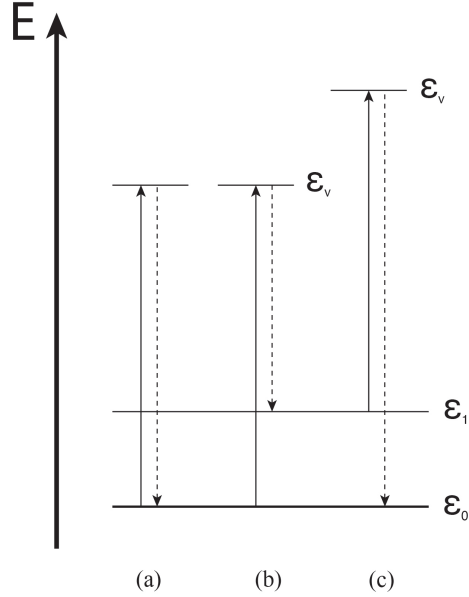
Figure 3.2: Three different scattering mechanisms: a) Rayleigh b) Stokes c) anti-Stokes.

3.2.1 Crystalline fraction evaluation

As a consequence of its long range order and the fact that the wave vector corresponding to the excitation is small compared to its Brillouin zone, crystalline silicon shows only one Raman active mode which is called the transverse optical mode (TO). Its signal is located at around 520 cm^{-1} in the spectrum. On the contrary, amorphous silicon shows no order and all the Raman modes are allowed. As a result a small peak below 400 cm^{-1} and a broader one at 480 cm^{-1} are shown by this kind of samples, the latter representing the TO-mode for a-Si.

When a sample is a mixture of the two phases (as the one produced in the work described in this thesis), it is possible to evaluate the percentage of each phase. The signal will have peaks produced by both the phases and a deconvolution method is needed to split the spectrum in two contributions. The model that has been used is the one proposed by Feldmann in his PhD thesis [4], based on a subtraction method. First, a factor A is calculated as:

$$A = 320\,\mathrm{cm}^{-1} \sum_{120\,\mathrm{cm}^{-1}}^{440\,\mathrm{cm}^{-1}} \left(\frac{I_{total}(\lambda)}{I_a(\lambda)} \right) \qquad (3.18)$$

Where $I_{total}(\lambda)$ is the intensity of the sample spectra and $I_a(\lambda)$ is the intensity of the reference a-Si spectra. Then a new spectra is obtained as:

$$I'_c = I_{total} - AI_a \qquad (3.19)$$

28

And the crystalline fraction can be easily evaluated as:

$$\rho = \frac{I_c'(520\,\mathrm{cm}^{-1})}{I_c'(520\,\mathrm{cm}^{-1}) + AI_a(520\,\mathrm{cm}^{-1})} \tag{3.20}$$

In Fig. 3.3 an example of the application of this process is shown.
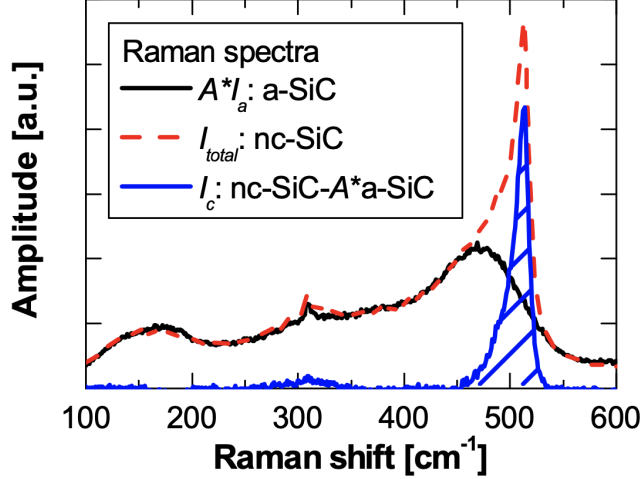
Figure 3.3: The corrected spectra is obtained subtracting the weighted amorphous spectra from the total spectra. Taken from [4].

3.3   Residual stress measurement

When a thin film is grown on a substrate which is made of a different material, the difference in thermal expansion coefficients, lattice dimension, and the eventual phase transformation and densification can be the cause of an internal residual stress build-up at the film-substrate interface. For example, consider a film-substrate composite in which there is no residual stress at the interface. After a temperature change the two layers will expand according to their thermal expansion coefficient, resulting in a different length variations. As the film layer is pinned to the substrate the different length variations will result in residual stress. The same consideration is valid also for mismatches of other properties such as the one listed before. Fig. 3.4 is the visual interpretation of the example previously done.

Residual stress can be the cause of film detachment or hillocks formation [26], its determination is then crucial to understand the blistering behaviour that has been shown by various films.
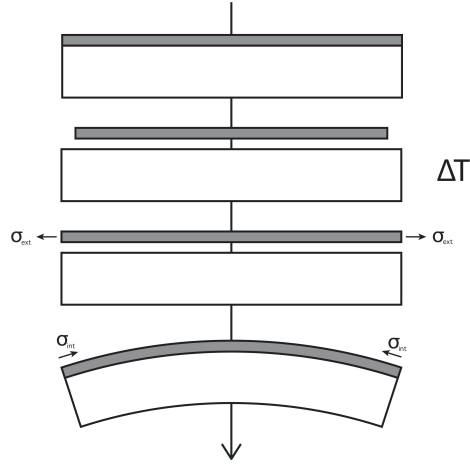
Figure 3.4: How thermal expansion coefficients mismatch causes residual stress when a temperature variation occurs: an external stress due to the pinning of the film-substrate composite is acting on the film, resulting in an internal stress with the opposite polarity.

3.3.1 Stoney formula

For the determination of the residual stress in the deposited film, the Stoney formula has been used:

$$\sigma = \frac{E_s}{6(1 - \nu_s)} \frac{h_s^2}{h_f} \left(\frac{1}{R} - \frac{1}{R_0} \right) \tag{3.21}$$

Where σ is the residual stress in the film, E_s is the Young's modulus of the substrate, h_s and h_f are, respectively, the thickness of the substrate and the thickness of the film and R is the curvature.

The original equation proposed by Stoney [27] did not take into account anisotropic substrates and multiple films. A corrected relation for single-crystal silicon substrates with (001) orientation that lays parallel to the film surface has been proposed by Janssen et al. [28]

$$\sigma = \frac{1}{6(s_{11}^{Si} + s_{12}^{Si})} \frac{h_s^2}{h_f} \left(\frac{1}{R} - \frac{1}{R_0} \right) \tag{3.22}$$

Where s_{11}^{Si} and s_{12}^{Si} are elements from the compliance tensor of silicon.

The value $1/(s_{11}^{Si} + s_{12}^{Si})$ is called the biaxial modulus of silicon which has the value of $1.803 \cdot 10^{11}$ Pa [28]. It is possible to conclude that, for this crystallographic orientation, curvature should be symmetrical, as the value of the biaxial modulus is the same in the two principal directions of the plane of the substrate.

3.3.2 Limit of validity

It is worth to note that the residual stress does not depend on any mechanical property of the film material. The reason for this relates to the derivation of the original equation and the assumpions that have been made. In practical cases, the thickness of the deposited film is 500 to 1000 times lower than the one of the substrate [26]. Under this condition it is possible to assume that the properties of the film-substrate composite are the one of the sole substrate. The formal validity condition to be satisfied is that the radius of curvature is large compared to the thickness of the composite [27].

3.3.3 Multiple film layers

With regards to multiple film layers, it comes from the previous consideration that, if the film is thin compared to the substrate, the flexural modulus of the composite is dominated by the one of the substrate. As a consequence, the properties of the film have a negligible weight into the total bending of the film/substrate. From these observations it is possible to conclude that, in case of subsequential depositions of thin films, the total bending is equal to the sum of the bending associated with each film as it was independent from the others [29][26]. In the practical case of 100 nm aSi(C,N,O)$_x$:H deposited after the growth of 1.6 nm of SiO$_x$ onto a 725μm-thick single crystal silicon substrate, the original radius of curvature R_0 is assumed to be the one of the Si/SiO$_x$ composite.

3.3.4 Curvature measurement

The radius of curvature of the samples has been calculated from the measurement of the bow of the wafers. For this purpose an ISIS SemDex301 by Sentronics Metrology has been used.

The tool is able to measure wafer bow that is the displacement of the wafer surface along the z coordinate assuming x-y is the plane on which the surface lays. For this scope the focusing distance of a near infrared light beam (wavelength of 1300nm) is measured. By combining the measured heights with the corresponding positions of the probe over the sample it is then possible to plot the entire surface profile.

To evaluate the two main radii of curvature (which are the one along the x axis and the one along the y axis) first the profile of the wafer surface is plotted for $x = 0$ and for $y = 0$, then the equation of the parabola that best fits the profile is found, as showed in Fig. 3.6. Recalling the formula of the curvature K of a curve that reads:

$$K(x) = \frac{|y(x)''|}{(1 + y(x)'^2)^{\frac{3}{2}}} \tag{3.23}$$

It is then easy to find that, at its vertex $(-\frac{b}{2a}; -\frac{\Delta}{4a})$, the curvature of the generic

31
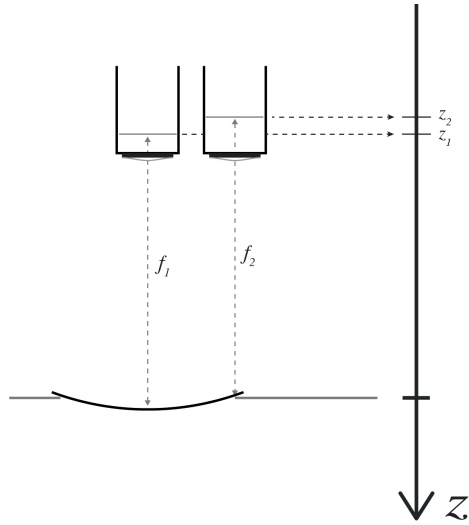
Figure 3.5: ISIS SemDex301 schematics: to be noticed the z axis orientation.

parabola $y(x) = ax^2 + bx + c$ is:

$$K\left(-\frac{b}{2a}\right) = 2a \qquad (3.24)$$

From the relation $K = \frac{1}{R}$ the radius of curvature is then found.

In all of the measurements the effect of gravity on the curvature has been neglected as the deposited film mass is considered negligible compared to the mass of the substrate. The resulting change in curvature is then assumed to be 0.
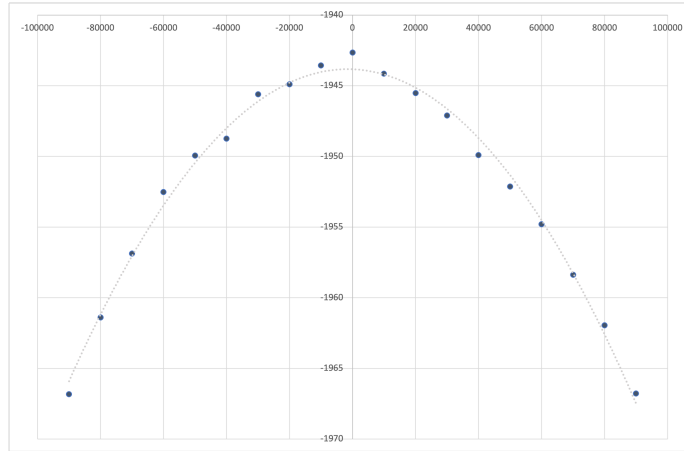
Figure 3.6: Example of the plot derived from the process of curvature evaluation, the dotted line corresponds to the parabolic fit of the bow profile.

Chapter 4

Production Technology

In this chapter, an overview on the techniques used to fabricate poly-Si passivated contacts will be presented. Afterwards, the main industrial production route for TOPCons will be described along with the motivation of researching on a possible alternative. Finally, a description of the tools used in this work will be presented.

4.1 SiO$_x$ growth

In most of the cases and in the work presented here, the interfacial passivation layer is made of sub-stoichiometric silicon oxide (SiO$_x$) which is grown to a thickness in the range of 1-3 nm [1]. SiO$_x$ can be thermally grown in a tube furnace at 550 °C-700 °C in O$_2$ atmosphere [1], [30], [31], chemically grown by immersion in hot nitric acid [32] or grown by either a UV/O$_3$-induced photo-oxidation or a bath in de-ionized ozonated water (DIO$_3$). In the latter case, thermally more stable interfacial layers are obtained which, in turn, improve surface passivation quality of n-type TOPCon [33] compared to the one obtained by immersion in hot HNO$_3$. Recent studies also exploited low-pressure chemical vapour deposition of the interfacial oxide along with the poly-Si deposition [34].

In general, all the techniques result in thin oxide layers with which J$_0$ values of less than 10 fA/cm^2 for both for n-type and p-type contacts can be reached [1].

4.2 Poly-Si deposition

In this section, an introduction to chemical vapor deposition (CVD), low-pressure chemical vapour deposition (LPCVD) and plasma-enhanced chemical vapour deposition (PECVD) will be given. Although poly-Si can be deposited by means of other CVD-derived techniques and physical vapour deposition (PVD), those techniques are not of interest for this work, thus they will not be reported.

4.2.1 Chemical vapour deposition

CVD is a technique widely used for thin-film deposition. The process that leads to material deposition is the reaction between two or more gaseous species or volatile compounds that produces a nonvolatile solid that can then deposit on a suitably placed substrate. Differently from physical vapor deposition (PVD) in which the source of the material is a solid which has to be evaporated by means of different mechanisms, CVD starts from vapor reactants, thus having an easier control on impurities and stoichiometry. The relative low cost for the equipment, in addition to the previously reported reasons, explains the popularity of the technique, specially in the semiconductor industry [5]. For the deposition of silicon films, the reaction involved is the pyrolysis of silane occurring at high temperatures: $\mathrm{SiH_{4(g)}} \longrightarrow \mathrm{Si_{(s)}} + 2\,\mathrm{H_{2(g)}}$ With this process, silicon is usually deposited either in amorphous or polycrystalline form. The two determining factors for the morphology of the growing film are the vapor saturation pressure and the substrate temperature. While the former has an effect on the nucleation rate of the deposit, the growth rate depends on the latter. A hot surface enhances adatoms mobility, thus promoting a crystalline growth. For instance, a silicon film produced on a substrate below 600 °C leads to amorphous silicon formation [5].

4.2.2 Low-pressure chemical vapour deposition

In LPCVD process the pressure in the deposition chamber is kept at values lower with respect to the atmospheric CVD processing, in particular values of 1 torr are found in LPCVD deposition chambers while the conventional CVD systems usually operate at around 760 torr [5]. With this technique it is possible to directly deposit poly-Si with a high control on impurities thanks to the low pressure in the chamber. The growth rates are higher with respect to the one of atmospheric-pressure CVD when normalized accordingly to the reactants' partial pressure. A typical LPCVD tool is represented in Fig. 4.1. The design of the chamber and the laminar flow of reactants, thank to the low pressure, allows to process multiple wafers at one time. On the other hand, directionality is lost and multiple masking or etching steps are required for single-side depositions. With this technology it is also possible to deposit in situ-doped poly-Si.
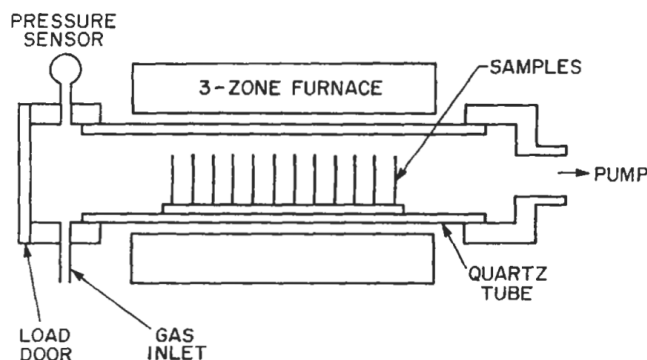
Figure 4.1: Scheme of a LPCVD deposition chamber. The wafer are stacked vertically in the quartz tube to prevent contamination from detachement of the wall deposit [5].

4.2.3 Plasma-enhanced chemical vapour deposition

The plasma-enhanced version of chemical vapor deposition is a fabrication technique that introduces plasma in the deposition chamber. In the case of semiconductor-dedicated processing tools, the glow discharge is promoted and sustained by a RF generator employing radio frequencies ranging from 100 kHz to 40 MHz. The energy of the discharge leads to the formation of very reactive radicals in the gas of reactants, thus promoting the deposition at temperatures lower than the usual ones. The main advantage of this technique is the possibility of depositing metals and semiconductors on temperature-sensitive substrates. Moreover, the effect of the plasma discharge can ease the process of depositing alloys. With this technique, it is possible to obtain amorphous silicon from silane even at temperatures lower than 200 °C [5]. As said before, plasma discharge promotes the generation of reactive species. In the case of silane, those species range from clusters of silicon atoms to Si-H complexes. As a result, the deposited film incorporates hydrogen in its structure [35], [36]. The so-obtained hydrogenated silicon has been widely used in photovoltaic industry since its first production. The advantage of using hydrogenated amorphous silicon (a-Si:H) for photovoltaics applications is the passivation efficiency of hydrogen atoms. The amorphous silicon deposited from standard CVD has a very high density of defects, and is thus not suitable for high-efficiency solar cells absorbers. On the other hand, PECVD a-Si:H results in a material with a significantly lower number of defects because of the hydrogen that passivates dangling bonds [37]. The incorporation of dopants and inclusions is also promoted by the almost defect-free structure formed thanks to hydrogen [38] [39]. Fig. 4.2 shows a typical PECVD chamber; the plasma discharge can only hit one side of the wafers, allowing single-side deposition.
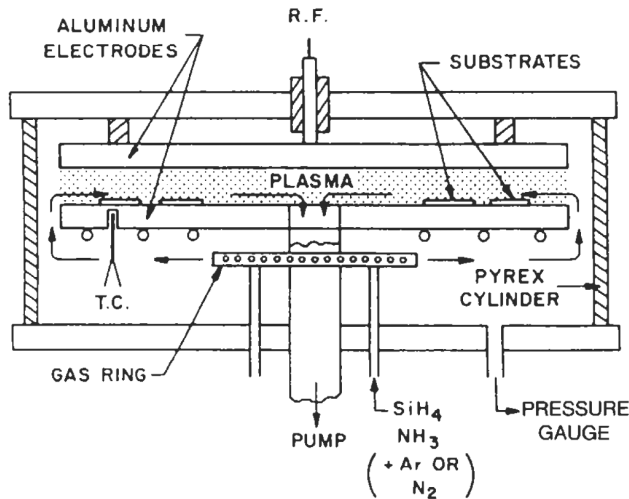
Figure 4.2: Scheme of a PECVD deposition chamber. The wafer are lying on a carrier, which acts as a mask, thus allowing single side deposition [5].

In the case of PECVD, an additional step of annealing is required to allow solid-phase crystallization of the amorphous hydrogenated silicon. This process leads to Si-H bond breakage and hydrogen release which can diffuse in the underneath layers, thus passivating surface and bulk defects.

4.3 Industrial production route of poly-Si passivated contacts

In industrial production lines, the use of tools already present in industry, and techniques capable of combining multiple production steps in one are preferable. In the case of the production of TOPCons, LPCVD is widely use for the production of the poly-Si layer, thanks to the high uniformity and consistency of it [40], [41]. On the other hand, the non-directional nature of the deposition requires multiple steps of masking and/or etching of one side of the wafer. PECVD is seen as a valid alternative due to the possibility of depositing poly-Si on one side only. Additionally, plasma-assisted deposition tools are already widely present in the production lines due to their use for SiN_x deposition in the last step before metallization.

While LPCVD can deposit polycrystalline silicon, the nature of the PECVD-deposited silicon is amorphous. In addition, hydrogen is incorporated in the layer. For this reason, an annealing step for solid-phase crystallization and hydrogen effusion is needed. If on one side, hydrogen enhances device quality by passivation of the defects at the SiO_x interfaces, on the other side, it is reported to be the cause of blister formation [9], [10], [40]. Research is being

performed in the production of blister-free poly-Si layers by PECVD, with some suggesting to add inclusion in the deposit [4], [12].

4.4 Tools overview

In this section, the tools used for the production of the samples needed for the experiment will be given.

4.4.1 Wafer preparation and oxide growth

Before processing, wafers were cleaned in a RENA Clean tool to remove the saw damage and the native silicon oxide. Oxide was grown either by wet-chemical oxidation in ozonated water or thermal oxidation in a TEMPRESS tube in O_2 atmosphere.

4.4.2 PECVD equipment

In the case of this work, two PECVD tools have been used for the deposition of 100 nm-thick a-Si$(C,N,O)_x$:H films, namely AK1000 and OPT. a-SiC$_x$:H was deposited with AK1000. Gas ratio and time were adapted to obtain a layer of the desired thickness. The power supplied by the RF generator was set to 600 W/m^2 and the temperature of the chamber was 200 °C. Methane was used to include carbon in the deposited layer, while for in situ P-doping, PH$_3$ was the gas of choice. a-SiN$_x$:H was deposited in OPT. The source of nitrogen was NH$_3$ and the power supplied was 936 W/m^2. The ratio of NH$_3$ with respect to SiH$_4$ was varied to change the inclusion of nitrogen in the deposit while the time of the deposition was tuned to reach thicknesses of 100 nm. For the deposition of a-SiO$_x$:H, the same procedure applied, with the difference of the use of N$_2$O instead of NH$_3$ to include oxygen in the deposit. In both cases, the chamber temperature was set to 250 °C. OPT did not allow in situ doping.

Lastly, SiN$_x$:H for hydrogenation of SiO$_x$/c-Si was deposited in a Tempress tube PECVD tool.

4.4.3 Annealing furnaces

Annealing was performed in a tube furnace by loading the wafers at 800 °C for 15 minutes for blistering test. In the case of solid-phase crystallization tests of non-blistering layers, instead, annealing was performed in a TEMPRESS automated tube in an N$_2$ environment.

Chapter 5

Blistering and residual stress of PECVD Si films

As was said in the previous chapters, the main drawback in the production of tunnel-oxide passivating contacts through the PECVD route is the blistering of the a-Si:H layer during its solid-phase crystallization. It has been observed in literature and in previous runs that by incorporating adequate amounts of certain inclusions, namely carbon, nitrogen and oxygen, it is possible to suppress blister formation in the layer [4], [12]. As shown by Malerba et al. in the study of Cu_2ZnSnS_4 layers, it is possible to correlate the blistering extent of the layers to their residual stress level [42]. To verify this theory in our case, an experiment was performed, with the scope of evaluating the residual stress state correlation with inclusion content and blistering extent.

5.1   Design of the experiment

For this study, samples as shown in Fig. 5.1 were made. The substrate of choice was a [001] mirror-polished, B-doped, 200 mm-diameter silicon wafer. The oxide was grown by wet-chemical oxidation in ozonated water, while the Si layer was grown by PECVD using SiH_4 and H_2. The precursor gases for C, N, and O inclusion in the layers were CH_4, NH_3, and N_2O, respectively.
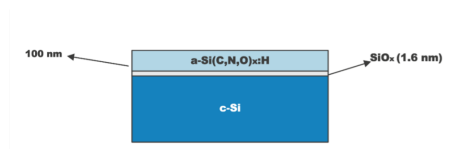

Figure 5.1: The resulting sample after wet-chemical oxidation and PECVD.

The important deposition parameters for the C-incorporated (a-SiC$_x$:H), N-incorporated (a-SiN$_x$:H), and O-incorporated (a-SiO$_x$N$_y$:H) Si layers are re-

ported in Table 5.1, Table 5.2, and Table 5.3, respectively. Before PECVD, the curvature of all the wafers was measured. For one of the samples, D01, the wet-chemical oxide was removed in dilute HF before PECVD in order to observe blistering extent in layers with no SiO_x underneath.

Sample ID	Gas flow ratio	Deposition temperature	Nominal thickness
D01	0.0	200 °C	100 nm
D02	0.0	200 °C	100 nm
D03	0.4	200 °C	100 nm
D04	0.8	200 °C	100 nm
D05	1.2	200 °C	100 nm
D06	1.6	200 °C	100 nm
D07	2.0	200 °C	100 nm

Table 5.1: Deposition parameters for a-SiC$_x$:H layers.

Sample ID	Gas flow ratio	Deposition temperature	Nominal thickness
D08	0.0	250 °C	100 nm
D09	0.1	250 °C	100 nm
D10	0.16	250 °C	100 nm
D11	0.26	250 °C	100 nm

Table 5.2: Deposition parameters for a-SiN$_x$:H layers.

Sample ID	Gas flow ratio	Deposition temperature	Nominal thickness
D12	1.1	250 °C	100 nm
D13	1.2	250 °C	100 nm
D14	1.3	250 °C	100 nm
D15	1.4	250 °C	100 nm
D16	1.5	250 °C	100 nm

Table 5.3: Deposition parameters for a-SiO$_x$:H layers.

The composition of the as-deposited layers was determined by elastic recoil detection (ERD) measurements. The as-deposited samples were annealed in a furnace for 15 minutes at 800 °C and later inspected under an optical microscope for blistering. The blistering severity was quantified by image processing with the imageJ software. Blister size, and blister coverage, i.e., the percentage of the total area covered by blisters, were the two parameters of choice to quantify the extent of blistering.

5.2   Results and discussions

First, we will present the results of the blistering analysis of the samples and then, of the residual stress measurements in the as-deposited layers.

5.2.1   Blistering behavior and layer composition

Fig. 5.2 shows the optical images of blistered samples while in the graph in Fig. 5.3 the blistering extent of all the samples produced is summarized. The pure a-Si:H films blistered severely with 40 % of the layer area blistered. The blistering severity decreased with increasing amount of precursor gas-to-SiH$_4$ flow ratio. A suppression of blistering was noticed after a certain amount of precursor gas-to-SiH$_4$ flow ratio. In particular, blisters did not form starting from samples with 1.6 $\dot{Q}_{CH_4/SiH_4}$, 0.26 $\dot{Q}_{NH_3/SiH_4}$ and 1.3 $\dot{Q}_{N_2O/SiH_4}$. Also, sample D01, which did not have an underlying SiO$_x$ layer, did not show any blister after annealing. In the case of a-SiC$_x$:H and a-SiN$_x$:H layers, the maximum blister size was observed to increase with the increasing amount of precursor gas-to-SiH$_4$ flow ratio. In the case of a-SiO$_x$:H layers, on the other hand, a decreasing trend is observed with respect to the increasing amount of precursor gas-to-SiH$_4$ flow ratio. As the precursor gas-to-SiH$_4$ flow ratio increases, an increase in the actual atomic concentration of inclusion in the layers is also seen. In Fig. 5.3 it is also possible to observe the inclusion content correspondence with the precursor gas-to-SiH$_4$ ratios on the upper X axes. In the case of a-SiO$_x$:H layers, besides oxygen, nitrogen is also incorporated at different ratios and a more detailed description of the composition with respect to the precursor gas-to-SiH$_4$ flow ratio is needed, which can be found in Fig. 5.4.

$\dot{Q}_{CH4}/\dot{Q}_{SiH4}$

0.0   0.4   0.8   1.2   1.6

$\dot{Q}_{NH3}/\dot{Q}_{SiH4}$

0.0   0.10   0.16   0.26

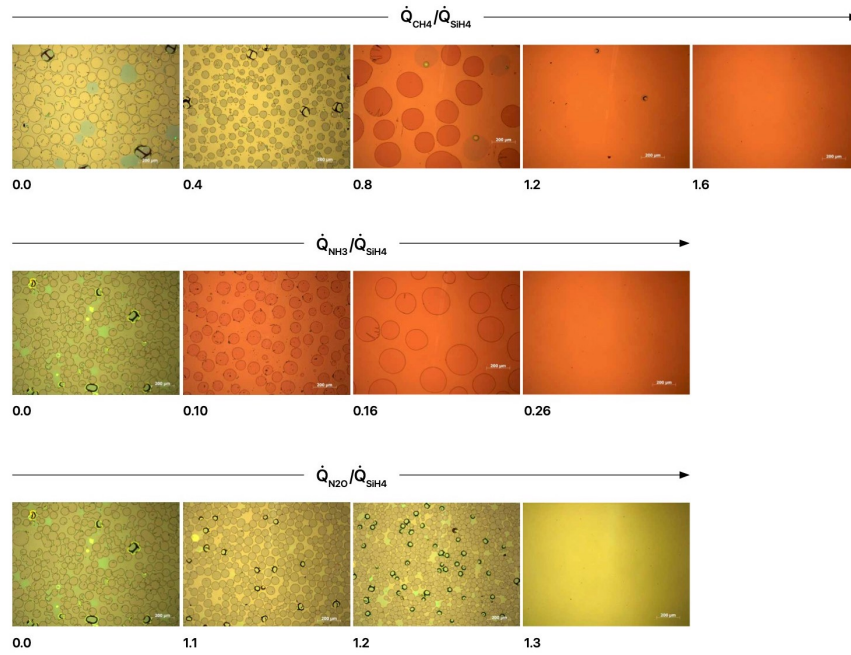$\dot{Q}_{N2O}/\dot{Q}_{SiH4}$

0.0   1.1   1.2   1.3

Figure 5.2: Optical images of the samples after annealing. Images of some of the samples which did not blister are omitted.

Figure 5.3: Blistering extent in (a) a-SiC$_x$ layers, (b) a-SiN$_x$ layers and (c) a-SiO$_x$N$_y$ layers. The blister area coverage is reported on the left axes while the blisters average size is reported on the right axes.
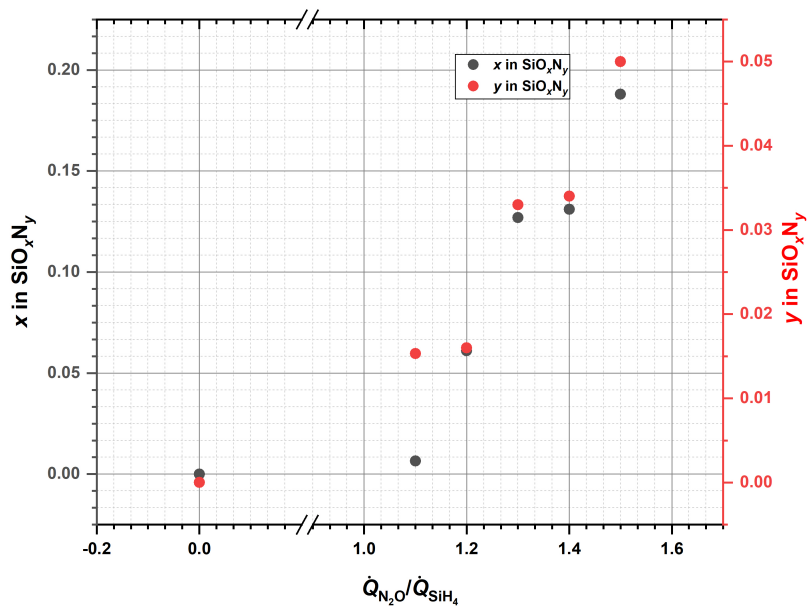
Figure 5.4: Inclusions content with respect to flow ratios for $aSiO_xN_y$:H layers.

In $a\text{-}SiC_x$:H and $a\text{-}SiN_x$:H layers, hydrogen concentration increased with the increase of precursor gas-to-SiH_4 flow ratio. This is due to additional H incorporation in the layers in the form of -C-H, -N-H, and -O-H bonds. Fig. 5.5 compares hydrogen content with the blistering extent of the layers. By looking at the graph it is possible to notice that the non-blistered layers present a significantly higher hydrogen content with respect to the one which blistered. Sample D06, for example, did not present any blister even if its H atomic concentration was 0.353, which is almost double compared to the 0.18 of sample D02 which had 43.45 % of its surface blistered.
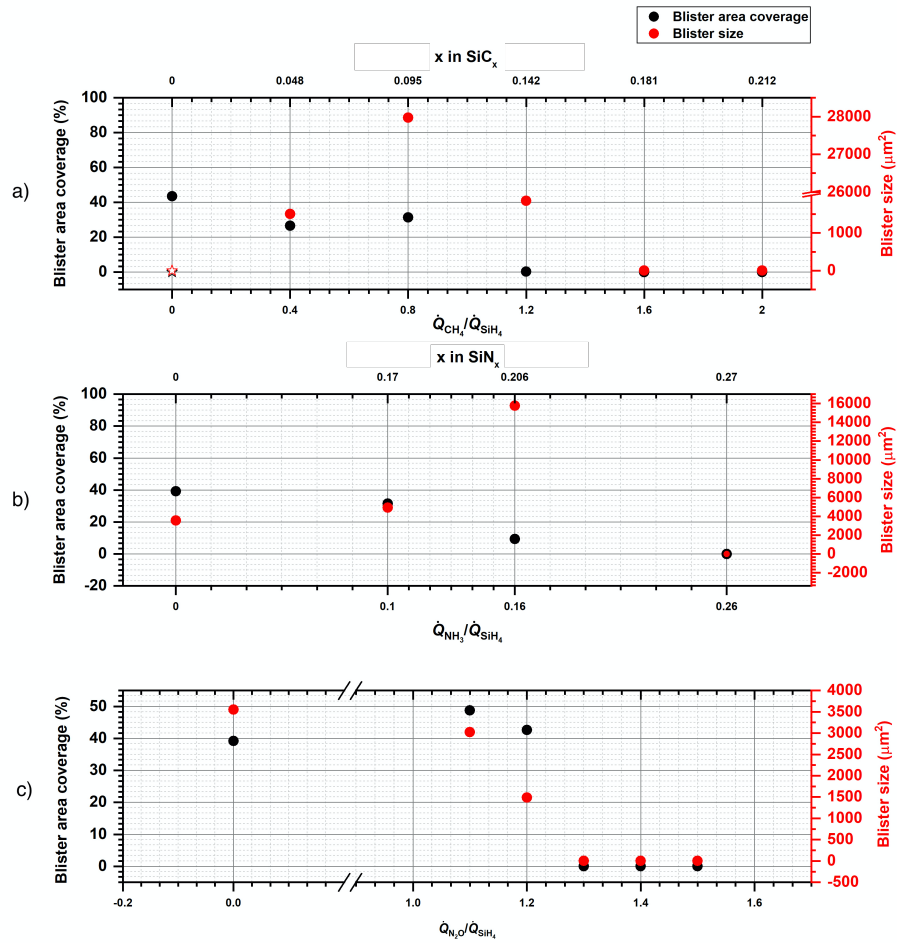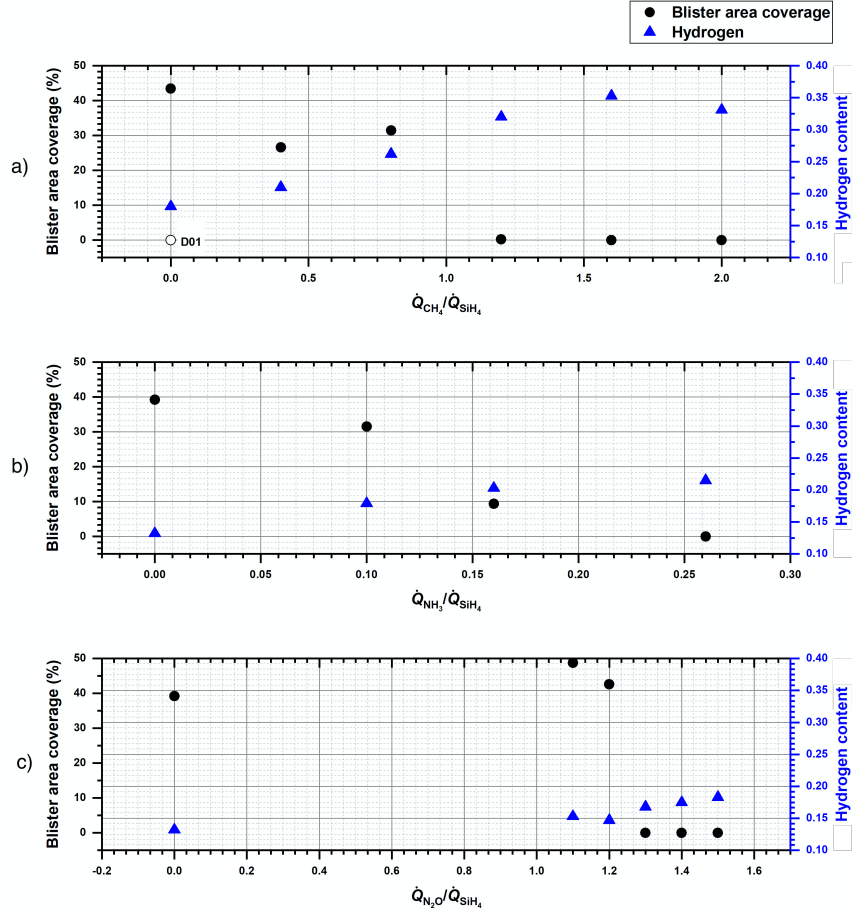
Figure 5.5: Hydrogen content and blistering extent in (a) a-SiC$_x$ layers, (b) a-SiNx layers and (c) a-SiO$_x$ layers. The blistering extent is reported on the left axes while the hydrogen atomic fraction is reported on the right axes.

5.2.2 Residual stress

In Fig. 5.6, the residual stress of the various as-deposited and annealed layers is listed vs. precursor gas-to-SiH$_4$ flow ratio. All the layers are in compressive residual stress. The values of the stress in the two principal directions are not perfectly equal as they should be. However, this can be attributed to nonuniformities of the deposited layers thickness along all the directions. Considering that the residual stress values along the X and Y axes differ by relatively small

amounts, the measurement methods and the approximation of biaxial stress state are still considered reliable. The data shows a decrease in the compressive residual stress as the precursor gas-to-SiH$_4$ flow ratio flow ratio increases. It is also possible to see that almost no difference in the stress is measured after a certain value of the precursor gas-to-SiH$_4$ flow ratio is reached. In particular, a-SiC$_x$:H layers reached a plateau of -400 MPa of stress, a-SiN$_x$:H ones for -270 MPa and a-SiO$_x$:H layers for -300 MPa. By looking at the values measured for sample D01 (represented as stars in Fig. 5.6), it is possible to conclude that the thin wet-chemical oxide has no significant effect on the residual stress.

Figure 5.6: Residual stress in the as-deposited (a) a-SiC$_x$ layers, (b) a-SiN$_x$ layers and (c) a-SiO$_x$ layers. The residual stress is reported on the left axes, the residual stress of non-blistered layers after annealing is pointed by arrows.

A correlation between blister-area coverage and residual stress was noticed and it is reported in Fig. 5.7. In particular, blisters were suppressed for values of residual compressive stress of 420 MPa for a-SiC$_x$:H, 268 MPa for a-SiN$_x$:H

layers and 440 MPa for a-SiO$_x$:H layers. After annealing, the samples which did not present blisters were measured again to evaluate their final residual stress. The results are showed in Fig. 5.6. It is possible to conclude that annealing has a stress relieving function, leaving the samples with a tensile residual stress which was measured in the range of 58 MPa to 257 MPa. The change in the residual stress sign could be a consequence of the loss of hydrogen and the solid-state crystallization, which could have lead to a decrease in the specific volume.
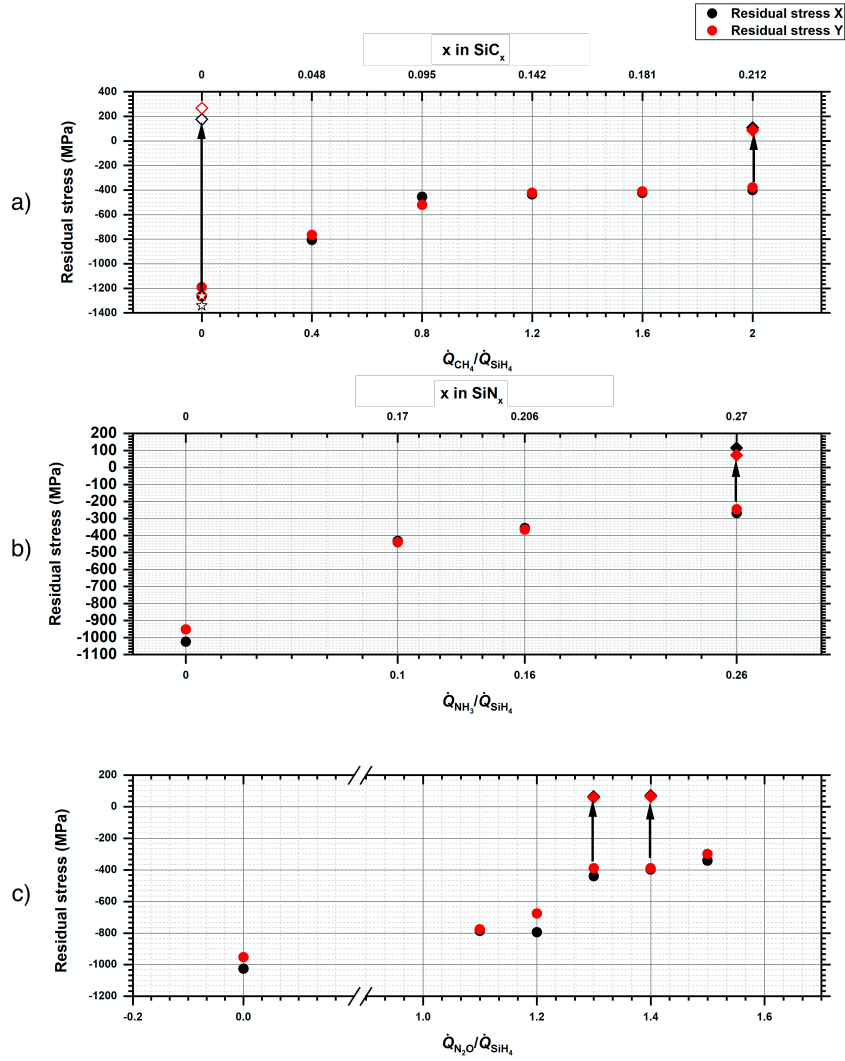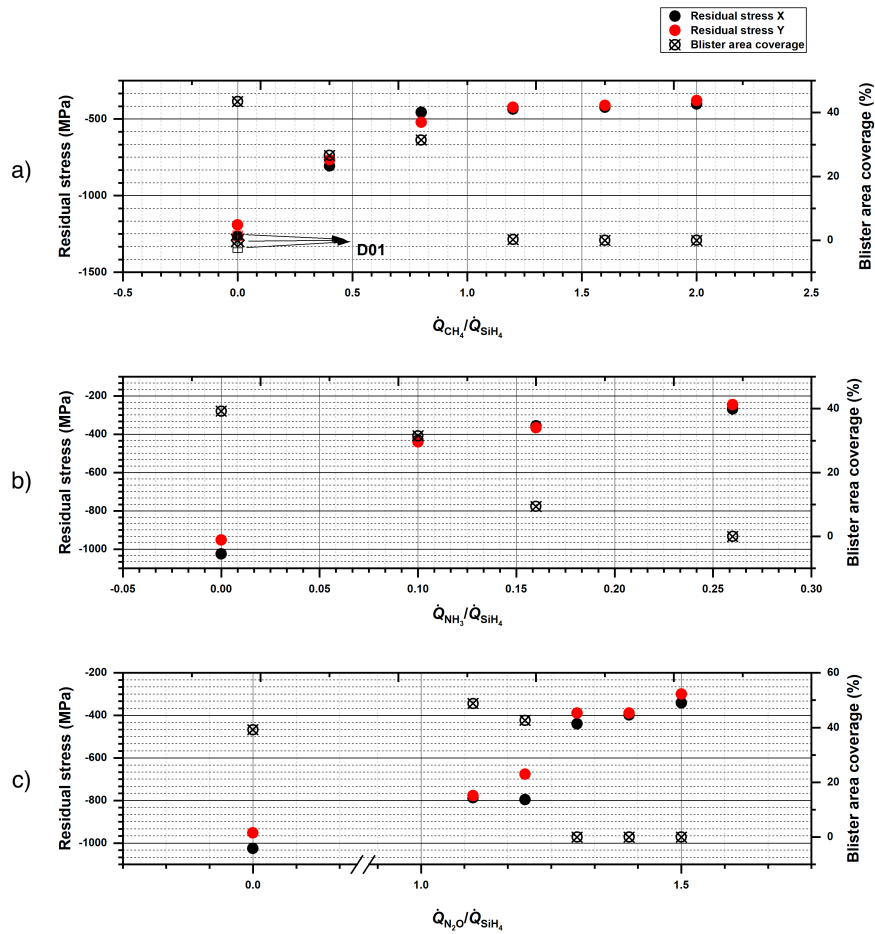

Figure 5.7: Comparison between residual stress and blistering extent in (a) a-SiC$_x$ layers, (b) a-SiN$_x$ layers and (c) a-SiO$_x$ layers. The residual stress is reported on the left axes while the blistering extent (evaluated through the area coverage) is reported on the right axes.

From the above data, hydrogen concentration in the layers seems to have no crucial influence on the extent of blistering. On the other hand, a direct correlation between residual stress and blistering is observed. Some deductions regarding the blistering mechanism can be made from this experimental evidence.

During fabrication, films are subjected to two treatments that are sources of residual compressive stress, which could be the main cause of blistering. The first compressive stress is accumulated during layer deposition while the second is accumulated during the initial phase of annealing, so when the temperature has not yet reached the window in which it is possible to observe hydrogen release and solid-state crystallization.

The stress accumulated during deposition is due to mismatches of various nature as explained in Chapter 3. From the data found in literature, it is possible to evaluate the contribution to the residual stress due to mismatch in the coefficients of thermal expansion (CTE) of the film and the substrate. The relation to calculate the thermal stress is given by Eq. 5.1:

$$|\sigma| = \frac{E_{film}}{1 - \nu_{film}}(\alpha^{film} - \alpha^{sub})\Delta T \tag{5.1}$$

Where α^{film} and α^{sub} indicates the CTEs of the film and the substrate. The material with the higher CTE expands more with respect to the other, thus accumulating tensile stress at its free surface, while the material with the lower CTE accumulates compressive stress at its free surface. Considering the CTE of amorphous hydrogenated silicon materials to be around $1 \cdot 10^{-6}$ K^{-1} [43], lower with respect to the one of the silicon substrate (which is $\sim 2.5 \cdot 10^{-6}$ K^{-1} [43]), the stress in the film is compressive and its value is in the order of tenths of 10^7 Pa. These values are significantly lower compared to the residual stress found in the produced films, thus it is possible to conclude that thermal stress is not the main contributor to the total residual stress in the films.

By looking at the three pure a-Si:H samples, namely D01, D02 and D08, a non-negligible difference in the residual stress after deposition is noticeable. In particular, D08 shows a compressive stress value of ~ 400 MPa lower compared to the other two samples, even if its deposition was performed at a higher temperature (250 °C as against 200 °C for D01 and D02). In this case, the higher chamber pressure (2 mbar with respect to 1.7 mbar used for D01 and D02) decreased the residual stress as confirmed by Iliescu et al. [44]. The magnitude of the residual stress decrease due to higher processing pressure is probably predominant with respect to the increase in the thermal stress.

The tendency towards less compressive residual stresses with the increasing precursor gas-to-SiH$_4$ flow ratio can be attributed to the rising inclusion content as shown by Sanders for a-SiC:H [45]. More specifically, the dependence can be justified by the variation of the depositing layer's structure and mechanical properties occurring with the introduction of carbon, nitrogen or oxygen atoms. In particular, changes in the defect density and microstructure as found by Petrich et al. for aSiC$_x$:H [46] could justify lower residual stress. In addition,

changes in the value of the Young's modulus or in the CTE, which are expected when changing the composition of the material, could have led to a decrease in the value of the thermal stress experienced by the layers after deposition [47], [48].

Another source of stress is the pressure generated by hydrogen accumulation at the film/oxide interface. In this case, too little data regarding the blisters volume, hydrogen molar density and H_2 concentration in the layers are available to evaluate at least the order of magnitude of this contribution. The works of Choi et al. [9] and Morriset et al. [10] confirm that the presence of hydrogen is essential in the blistering process.

To conclude, in the case of D01, the absence of blisters can be explained by the absence of a hydrogen diffusion barrier (namely, the wet-chemical oxide) that could have promoted hydrogen diffusion to the substrate instead of hydrogen accumulation at the a-Si/SiO_x interface [9].

5.3 Conclusions

In this experiment, the composition and residual stress of C-incorporated, N-incorporated and O-incorporated Si layers were analysed. Blistering suppression was obtained in layers with high inclusion content. A possible explanation of the major causes of blistering was given which relies on residual stresses accumulated by layers during fabrication.

Chapter 6

Study on properties of SiO$_x$-based contacts made with non-blistering PECVD a-Si(C,N,O)$_x$ layers

This part of the work aims to examine the surface passivation quality of non-blistering PECVD a-Si(C,N,O)$_x$ layers namely SRC2.0 (C-included, deposited with $\dot{Q}_{CH_4/SiH_4} = 2.0$), SRN0.26 (N-included, deposited with $\dot{Q}_{NH_3/SiH_4} = 0.26$) and SRO1.3 (N,O-included, deposited with $\dot{Q}_{N_2O/SiH_4} = 1.3$), in SiO$_x$-based passivating contacts. As a reference, the layers will be compared with LPCVD poly-Si. This will be examined for a range of annealing temperatures. Also, the microstructure of the layers for different annealing temperatures will be studied by Raman spectroscopy. Finally, a comment on the possibility of application of the PECVD layers will be presented.

6.1   Design of the experiment

For the evaluation of the surface recombination characteristic of the contact, symmetrical samples, as depicted in Fig. 6.1, with each of the SRC2.0, SRN0.26, SRO1.3 and poly-Si layers were produced. The substrate of choice was saw-damage-etched (SDE), P-doped crystalline silicon (c-Si) wafer with a thickness of around 175 μm and a resistivity of 4.4 Ωcm. After cleaning the wafers in a wet-chemical bath, a 1.6 nm-thick SiO$_x$ layer was grown via thermal oxidation. Next, around 100 nm-thick undoped SRC2.0, SRN0.26 or SRO1.3 layer was deposited on both sides of the wafer, while poly-Si layer was grown via LPCVD. Then the samples were annealed at different temperatures ranging from 850 °C to 950 °C for 30 min. Finally, a-SiN$_x$:H (refractive index n = 2.04 at 633 nm) was

deposited via PECVD on both sides for hydrogenation of the c-Si/SiO$_x$ interface. Photoconductance decay (PCD) and photo-luminescence (PL) measurements of the samples were then performed and their surface recombination velocities (SRVs) were determined.
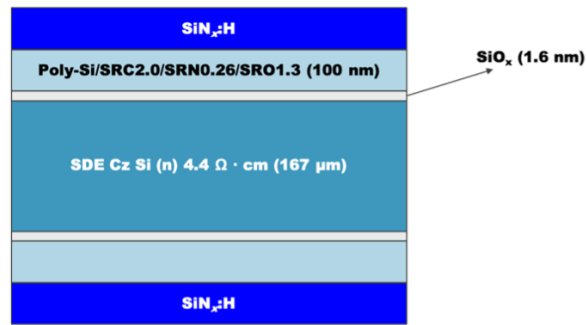

Figure 6.1: Schematics of the sample structure used for evaluating surface recombination properties via PCD measurements.

Table 6.1 reports the specifications of the various samples produced.

Sample ID	Layer type	Annealing temperature
D01		850 °C
D02		875 °C
D03	LPCVD Si	900 °C
D04		925 °C
D05		950 °C
D06		850 °C
D07		875 °C
D08	SRC2.0	900 °C
D09		925 °C
D10		950 °C
D11		850 °C
D12		875 °C
D13	SRN0.26	900 °C
D14		925 °C
D15		950 °C
D16		850 °C
D17		875 °C
D18	SRO1.3	900 °C
D19		925 °C
D20		950 °C

Table 6.1: Specifications of the samples for evaluating the surface recombination velocity of various layers in combination with thin thermal SiO_x in this study.

After the PCD measurements, the a-SiN_x:H layer of the samples was etched off in dilute HF and the SRC2.0, SRN0.26, SRO1.3 and poly-Si layers were characterized by Raman spectroscopy. The Si crystallinity of the layers was then evaluated from their respective Raman spectrum as described in the Metrology chapter.

In another study, as-deposited samples, as shown in Fig. 6.1, were doped with P by diffusion with $POCl_3$ at 850 °C; the dopant drive-in time was 40 min. Table 6.2 shows the overview of these samples. The recombination current density prefactor (J_0) of these samples was determined from PCD measurements.

Sample ID	Layer type	Diffusion temperature
D21	LPCVD Si	
D22	SRC2.0	
D23	SRN0.26	850 °C
D24	SRO1.3	

Table 6.2: Processing parameters for samples D21-D24.

6.2 Results and discussion

6.2.1 Undoped samples

Samples D01-D05 could reach injection level (Δn) of 10^{16} cm^{-3} and above and the method of determining SRV as described in Chapter 3 was used for them. However, for samples D06-D20 high carrier injection levels could not be reached and thus, the SRV of these samples was determined by taking the lifetime value at the highest carrier injection in Eq. 3.11. The measured SRVs for samples D01-D20 are reported in Fig. 6.2. As it is possible to observe, samples with SRC2.0, SRN0.26 or SRO1.3 layers showed SRVs in the order of thousands of cm/s, while SRVs in the order of a few cm/s were obtained for samples with LPCVD poly-Si layers. For the latter, a minimum was obtained with annealing at 900 °C. The increase in SRV above 900 °C can be linked to a degradation of the thin SiO$_x$ layer [49]. The very high SRVs of samples with PECVD layers for all annealing temperatures is indicative of a high concentration of defects at the c-Si/SiO$_x$ interface.
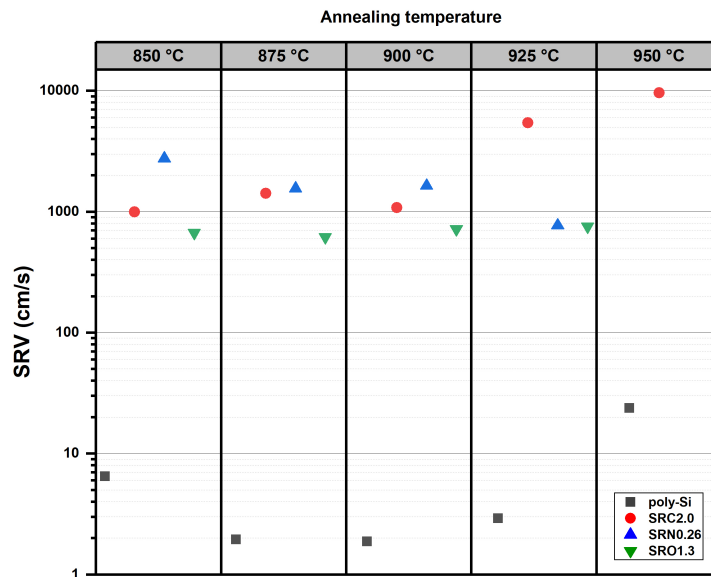

Figure 6.2: SRV measurements of samples D01-D20.

6.2.2   Doped samples

Fig. 6.3 shows the measured values of J_0 for samples D21-D24. The lowest value of J_0 was measured for the LPCVD poly-Si sample D21, the highest value was measured for the SRO1.3 sample D24. The J_0 value of D22 was found to be low and comparable to other samples, however, its inverse corrected lifetime curve had an unusually high value compared to that of the other samples for all injection levels (Δn) as shown in Fig. 6.4. For $\Delta n = 10^{15}$ cm^{-3}, the lifetime of D22 was measured to be 433 μs, which is one order of magnitude lower with respect to the highest lifetime measured that is 4270 μs for sample D21. The short lifetime of D22 suggests that low injection condition was not present at the surface and thus, the use of J_0 to describe its surface recombination characteristic might not be appropriate. This could be the case if there was no dopant diffusion into c-Si for this sample.
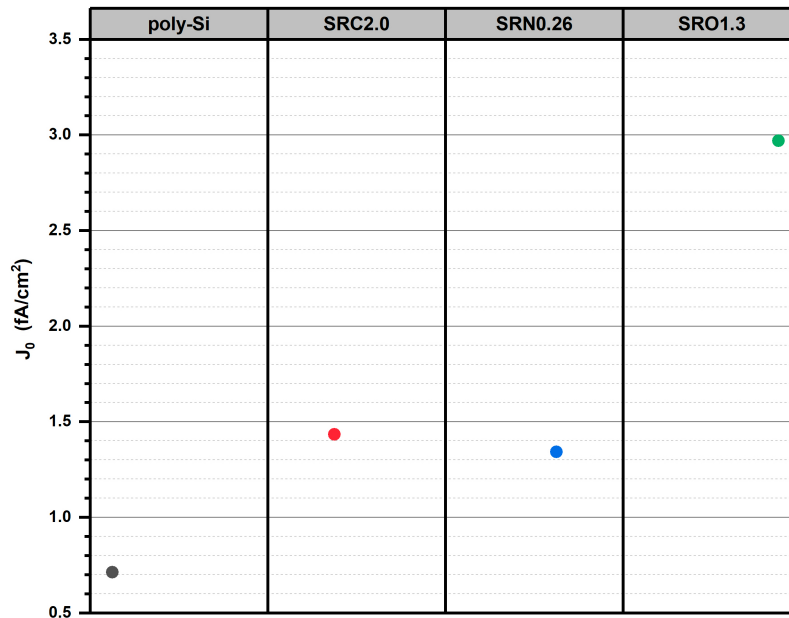

Figure 6.3: Recombination prefactor J_0 for samples D21-D24.
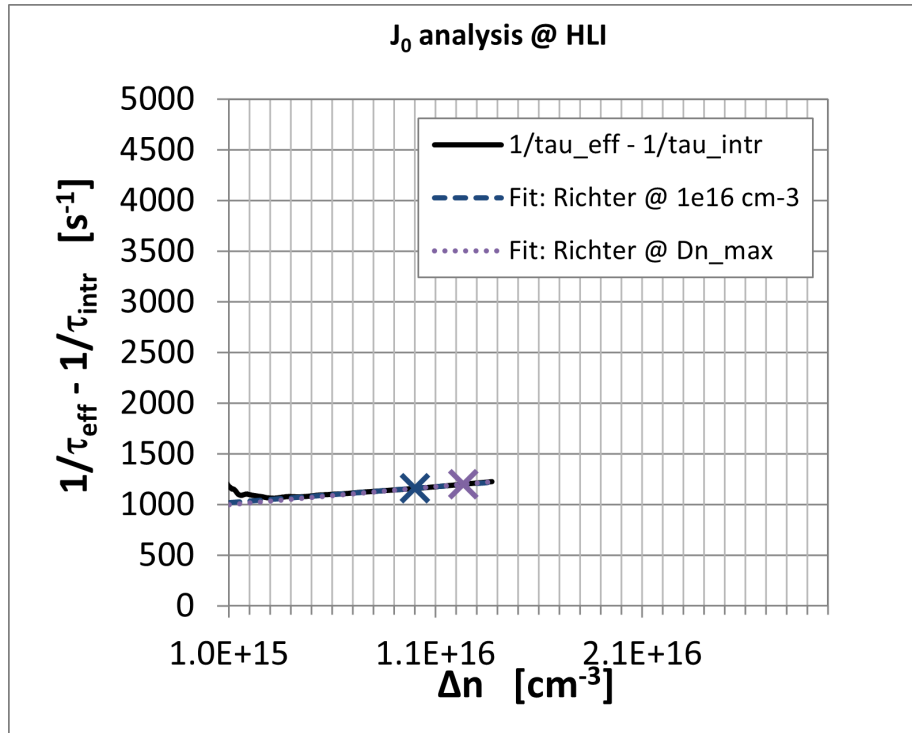
Figure 6.4: Inverse corrected lifetime for sample D22.

6.2.3 Photoluminescence measurements
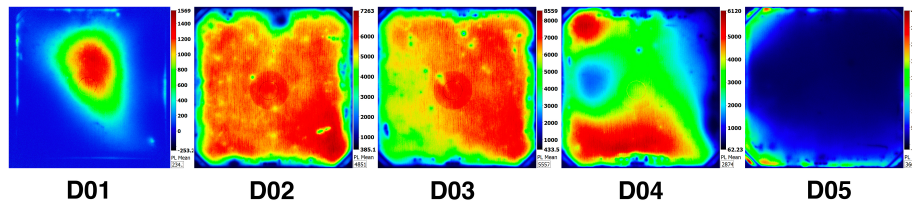
Figure 6.5: PL imaging of samples D01-D05.

As it is possible to see in Fig. 6.5, PL intensities were non uniform across the wafers except for sample D02. The reasons for this behavior are not known. Regarding the samples D06-D20, the luminescence was too low to be detected and nothing can be told regarding the uniformity of the layers. Also in the case of the doped D21-D24 samples, photoluminescence imaging showed non uniformity in the passivation across the wafer surface, as shown in Fig. 6.6.
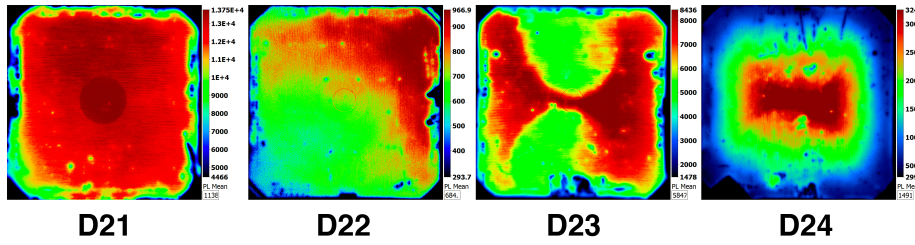
Figure 6.6: Photolumescence images of samples D21-D24.

6.2.4 Raman analysis

The spectra obtained by Raman spectroscopy for samples D01-D20 are showed in Fig. 6.7. From these spectra, the crystallinity of the excess Si, which is the amount of silicon which is not in a compound form with the inclusions, was evaluated.

Figure 6.7: Raman spectra of samples D01-D20.

By a first qualitative observation of the peak around 480 cm^{-1}, it is possible
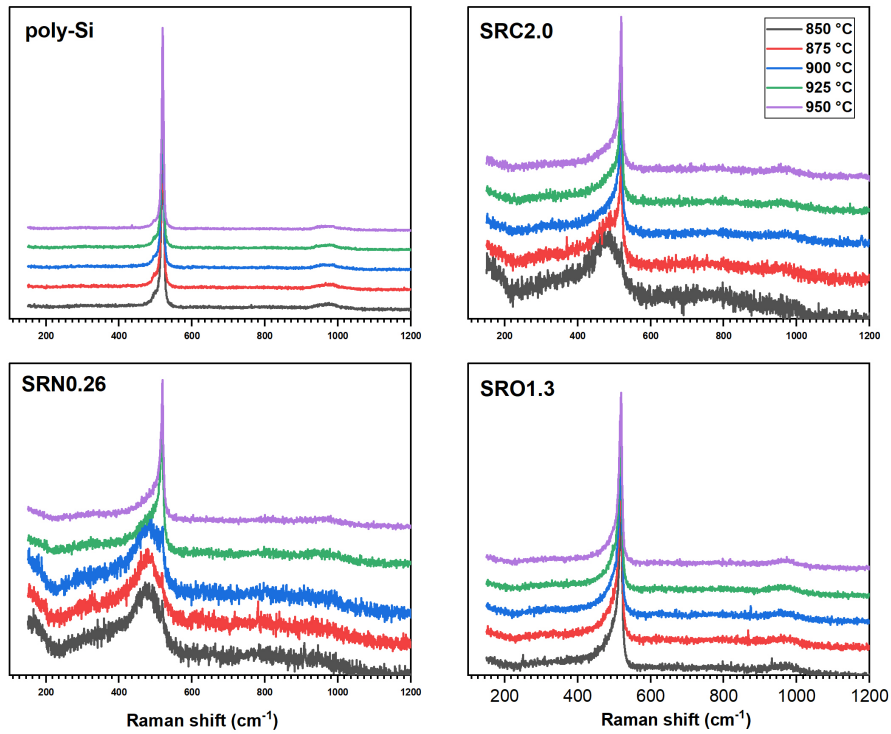
to notice that some samples remained completely amorphous, this is the case for SRC2.0 annealed at 850 °C and SRN0.26 annealed at 850 °C and 875 °C. The quantitative analysis of the data obtained is summarised in Fig. 6.8. As it is possible to notice, SRO1.3 reached a value of 90.2 % of crystallinity even with the lowest annealing temperature of 850 °C, while SRC2.0 and SRN0.26 required higher temperatures for initiation of crystallization. After the temperature threshold for crystallization was reached, all the samples showed increasing crystallinity with the increase in the annealing temperature. Ideally, a very high crystallinity is desired so as to have a high carrier concentration (this is mainly true for doped samples).
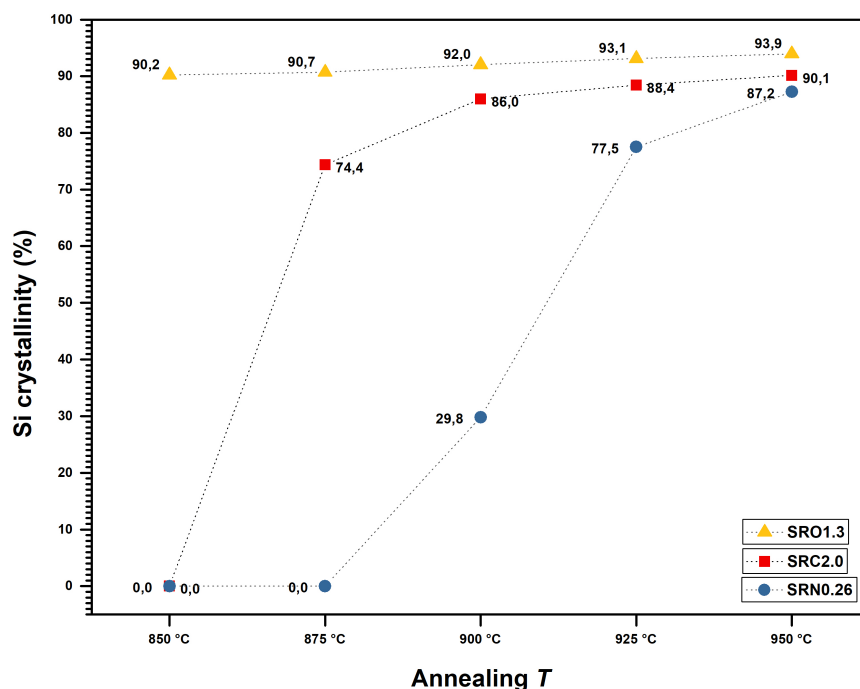
Figure 6.8: Crystallinity of samples D06-D20.

6.3 Conclusions

We found that ultra-thin thermal SiOx in combination with intrinsic LPCVD poly-Si shows much better surface passivation than with the intrinsic SRC2.0, SRN0.26 or SRO1.3 layers. Regarding the doped samples, the LPCVD poly-Si sample showed the lowest value of J_0 (0.7 fA/cm^2) after annealing at 850 °C. The sample with PECVD SRN0.26 layer was second-best showing J_0 value of 1.3 fA/cm^2. The SRO1.3 sample showed the highest value of J_0 of 2.9 fA/cm^2.

For a well passivated poly-Si/SiO$_x$ contact, J$_0$ values as low as 2 fA/cm^2 have been obtained [50], thus doped SRC2.0, SRN0.26, SRO1.3 layers can be considered to have reached a good passivation quality. Dopants increase the minority carrier potential barrier at the interface [18] and this could be the reason for the different quality measured for doped and undoped layers. In conclusion, for the application of these layers in passivating contacts, doping was demonstrated to be necessary to get low surface recombination. The passivation quality of such doped PECVD layers was measured to be lower but comparable to the intrinsic LPCVD poly-Si layer used as a reference. Further studies on the charge-carrier transport properties are needed to completely understand a possible future implementation of these layers in passivating contacts.

Chapter 7

Summary and outlook

7.1 Summary

High-efficiency solar cells are devices of utmost importance in the modern era. Recent advancements in the research have proven the high benefits of implementing the so-called passivated contacts in silicon devices and lab studies have registered record efficiencies of more than 25 % with cells featuring this technology. This thesis focused on poly-Si passivated contacts which are composed by a thin silicon oxide film underneath a highly doped poly-crystalline silicon layer. This relative simple architecture shows limitations for what concern its production route. Its fabrication process, indeed, could be significantly simplified by depositing an a-Si layer via PECVD starting from silane, which will be then annealed to allow hydrogen release (useful to passivate surface defects) and solid phase crystallization, instead of LPCVD, which is of higher costs and requires a higher number of steps. The problem of the PECVD route is the annealing step, which causes severe damage to the silicon layer by means of blister formation. It has been shown that blister suppression is possible with inclusion of carbon, nitrogen or oxygen in the silicon layer during PECVD.

This work studied the blistering of various a-Si(C,N,O)$_x$:H layers after deposition and annealing. The residual stress of the as-deposited layers was found to be compressive in all the cases, and the value of it was measured to be decreasing with the increase of the inclusion content in the layers. For each type of layer, blistering extent was measured to be lower in layers with lower residual compressive stress. Also, complete suppression of blistering was noticed after a certain residual stress value was reached. In non-blistering layers, hydrogen concentration was measured to be up to three times higher with respect to the blistering one, for this reason, even if hydrogen is clearly the main driving force for blistering to occur, its concentration was considered of low importance in the development of a blistering suppression strategy.

This work also explored the properties of SiO$_x$-based contacts made with non-blistering PECVD a-Si(C,N,O)$_x$:H layers. First, undoped layers showed

significantly lower passivation quality with respect to LPCVD undoped poly-Si layers. On the other hand, doped PECVD layers showed good values of J_0, with SRN0.26 showing the lowest value of 1.3 fA/cm^2. Also in this case, LPCVD poly-Si was the best layer, with a J_0 value of 0.7 fA/cm^2. Further studies are needed to evaluate if the lower passivation quality of PECVD layers can be compensated by their easier and cheaper production route.

7.2   Outlook

As demonstrated by this study, it is possible to obtain blister-free, Si-rich polycrystalline layers with the use of PECVD. Good results in term of J_0 value have been obtained with P-diffused SRC2.0, SRN0.26 and SRO1.3 layers, even if the lowest recombination prefactor was shown by the LPCVD poly-Si.

In future works, tests with different deposition parameters could be performed. As seen in this thesis, higher chamber pressures could lower the value of the residual stress, this way it could be possible to obtain blister-free layers with lower amount of inclusions, which, in turn, could be beneficial for the passivation quality and optical properties.

Other tests with in-situ, P-doped, PECVD a-Si(C,N,O)$_x$ could be performed so to evaluate the difference in the performance of in-situ and ex-situ doped layers. Also, in-situ doping would be preferred for industrial production optimization.

Lastly, an evaluation of the performance of these layers in actual devices could be carried out, with an evaluation of the reduction of the costs of the PECVD route compared to the LPCVD one.

Bibliography

[1] Di Yan, Andres Cuevas, Jesús Ibarra Michel, Chun Zhang, Yimao Wan, Xinyu Zhang, and James Bullock. Polysilicon passivated junctions: The next technology for silicon solar cells? *Joule*, 2021.

[2] Ralf B Wehrspohn, Uwe Rau, and Andreas Gombert. *Photon management in solar cells*. John Wiley & Sons, 2015.

[3] Abhijit S Kale, William Nemeth, Steven P Harvey, Matthew Page, David L Young, Sumit Agarwal, and Paul Stradins. Effect of silicon oxide thickness on polysilicon based passivated contacts for high-efficiency crystalline silicon solar cells. *Solar Energy Materials and Solar Cells*, 185:270–276, 2018.

[4] Frank Feldmann. *Carrier-selective contacts for high-efficiency Si solar cells*. PhD thesis, 2015.

[5] Milton Ohring. *Materials science of thin films*. Elsevier, 2001.

[6] Nancy M Haegel, Harry Atwater, Teresa Barnes, Christian Breyer, Anthony Burrell, Yet-Ming Chiang, Stefaan De Wolf, Bernhard Dimmler, David Feldman, Stefan Glunz, et al. Terawatt-scale photovoltaics: Transform global energy. *Science*, 364(6443):836–838, 2019.

[7] Energy production and consumption, Nov 2020. `https://ourworldindata.org/energy-production-consumption`.

[8] Kunta Yoshikawa, Hayato Kawasaki, Wataru Yoshida, Toru Irie, Katsunori Konishi, Kunihiro Nakano, Toshihiko Uto, Daisuke Adachi, Masanori Kanematsu, Hisashi Uzu, et al. Silicon heterojunction solar cell with interdigitated back contacts for a photoconversion efficiency over 26%. *Nature energy*, 2(5):1–8, 2017.

[9] Sungjin Choi, Ohmin Kwon, Kwan Hong Min, Myeong Sang Jeong, Kyung Taek Jeong, Min Gu Kang, Sungeun Park, Kuen Kee Hong, Hee-eun Song, and Ka-Hyun Kim. Formation and suppression of hydrogen blisters in tunnelling oxide passivating contact for crystalline silicon solar cells. *Scientific Reports*, 10(1):1–14, 2020.

[10] Audrey Morisset, Raphaël Cabal, Bernadette Grange, Clément Marchat, José Alvarez, Marie-Estelle Gueunier-Farret, Sébastien Dubois, and Jean-Paul Kleider. Highly passivating and blister-free hole selective poly-silicon based contact for large area crystalline silicon solar cells. *Solar Energy Materials and Solar Cells*, 200:109912, 2019.

[11] Yuguo Tao, Elizabeth Lori Chang, Ajay Upadhyaya, Brian Roundaville, Young-Woo Ok, Keeya Madani, Chia-Wei Chen, Keith Tate, Vijaykumar Upadhyaya, Francesco Zimbardi, et al. 730 mv implied voc enabled by tunnel oxide passivated contact with pecvd grown and crystallized n+ polycrystalline si. In *2015 IEEE 42nd Photovoltaic Specialist Conference (PVSC)*, pages 1–5. IEEE, 2015.

[12] Gizem Nogay, Josua Stuckelberger, Philippe Wyss, Esteban Rucavado, Christophe Allebé, Takashi Koida, Monica Morales-Masis, Matthieu Despeisse, Franz-Josef Haug, Philipp Löper, et al. Interplay of annealing temperature and doping in hole selective rear contacts based on silicon-rich silicon-carbide thin films. *Solar Energy Materials and Solar Cells*, 173:18–24, 2017.

[13] J. Bullot and M. P. Schmidt. Physics of amorphous silicon–carbon alloys. *physica status solidi (b)*, 143(2):345–418, 1987.

[14] W. Beyer, H. Wagner, and F. Finger. Hydrogen evolution from a-si:c:h and a-si:ge:h alloys. *Journal of Non-crystalline Solids*, pages 857–860, 1985.

[15] Peter Würfel and Uli Würfel. *Physics of solar cells: from basic principles to advanced concepts*. John Wiley & Sons, 2016.

[16] Jenny A Nelson. *The physics of solar cells*. World Scientific Publishing Company, 2003.

[17] Andres Cuevas and Di Yan. Misconceptions and misnomers in solar cells. *IEEE Journal of Photovoltaics*, 3(2):916–923, 2013.

[18] HyunJung Park, Hyomin Park, Se Jin Park, Soohyun Bae, Hyunho Kim, Jee Woong Yang, Ji Yeon Hyun, Chang Hyun Lee, Seung Hyun Shin, Yoonmook Kang, et al. Passivation quality control in poly-si/siox/c-si passivated contact solar cells with 734 mv implied open circuit voltage. *Solar Energy Materials and Solar Cells*, 189:21–26, 2019.

[19] AnYao Liu, Di Yan, Jennifer Wong-Leung, Li Li, Sieu Pheng Phang, Andres Cuevas, and Daniel Macdonald. Impurity gettering by diffusion-doped polysilicon passivating contacts for silicon solar cells. In *2018 IEEE 7th World Conference on Photovoltaic Energy Conversion (WCPEC)(A Joint Conference of 45th IEEE PVSC, 28th PVSEC & 34th EU PVSEC)*, pages 1667–1671. IEEE, 2018.

[20] JL Benton. Transition metals in silicon. 2001.

[21] Andres Cuevas and Daniel Macdonald. Measuring and interpreting the lifetime of silicon wafers. *Solar Energy*, 76(1-3):255–262, 2004.

[22] Ronald A Sinton, Andres Cuevas, and Michael Stuckings. Quasi-steady-state photoconductance, a new method for solar cell material and device characterization. In *Conference Record of the Twenty Fifth IEEE Photovoltaic Specialists Conference-1996*, pages 457–460. IEEE, 1996.

[23] Armin Richter, Stefan W. Glunz, Florian Werner, Jan Schmidt, and Andres Cuevas. Improved quantitative description of auger recombination in crystalline silicon. *Phys. Rev. B*, 86:165202, Oct 2012.

[24] Helmut Mäckel and Kenneth Varner. On the determination of the emitter saturation current density from lifetime measurements of silicon devices. *Progress in Photovoltaics: Research and Applications*, 21(5):850–866, 2013.

[25] Andres Cuevas. The recombination parameter j0. *Energy Procedia*, 55:53–62, 2014.

[26] William D Nix. Mechanical properties of thin films. *Metallurgical transactions A*, 20(11):2217, 1989.

[27] G. Gerald Stoney. The tension of metallic films deposited by electrolysis. *Proceedings of the Royal Society of London. Series A, Containing Papers of a Mathematical and Physical Character*, 82, 1909.

[28] Guido CAM Janssen, MM Abdalla, F Van Keulen, BR Pujada, and B Van Venrooy. Celebrating the 100th anniversary of the stoney equation for film stress: Developments from polycrystalline steel strips to single crystal silicon wafers. *Thin Solid Films*, 517(6):1858–1867, 2009.

[29] Jin S. Kim, Kyung W. Paik, and Seung H. Oh. The multilayer-modified stoney's formula for laminated polymer composites on a silicon substrate. *Journal of Applied Physics*, 86, 1999.

[30] Leonard Tutsch, Frank Feldmann, Jana Polzin, Christoph Luderer, Martin Bivour, Anamaria Moldovan, Jochen Rentsch, and Martin Hermle. Implementing transparent conducting oxides by dc sputtering on ultrathin siox/poly-si passivating contacts. *Solar Energy Materials and Solar Cells*, 200:109960, 2019.

[31] Manuel Schnabel, Bas WH Van De Loo, William Nemeth, Bart Macco, Paul Stradins, WMM Kessels, and David L Young. Hydrogen passivation of poly-si/siox contacts for si solar cells using al2o3 studied with deuterium. *Applied Physics Letters*, 112(20):203901, 2018.

[32] Jana-Isabelle Polzin, Frank Feldmann, Bernd Steinhauser, Martin Hermle, and Stefan W Glunz. Study on the interfacial oxide in passivating contacts. In *AIP Conference Proceedings*, volume 2147, page 040016. AIP Publishing LLC, 2019.

[33] Anamaria Moldovan, Frank Feldmann, Kai Kaufmann, Susanne Richter, Martina Werner, Christian Hagendorf, Martin Zimmer, Jochen Rentsch, and Martin Hermle. Tunnel oxide passivated carrier-selective contacts based on ultra-thin sio2 layers grown by photo-oxidation or wet-chemical oxidation in ozonized water. In *2015 IEEE 42nd Photovoltaic Specialist Conference (PVSC)*, pages 1–6. IEEE, 2015.

[34] Shubham Duttagupta, Naomi Nandakumar, Rolf Stangl, and Armin G Aberle. Initial results of monopoly tm silicon solar cells at seris. In *2018 IEEE 7th World Conference on Photovoltaic Energy Conversion (WCPEC)(A Joint Conference of 45th IEEE PVSC, 28th PVSEC & 34th EU PVSEC)*, pages 1991–1994. IEEE, 2018.

[35] Jérôme Perrin. Plasma and surface reactions during a-si: H film growth. *Journal of non-crystalline solids*, 137:639–644, 1991.

[36] J Perrin, O Leroy, and MC Bordage. Cross-sections, rate constants and transport coefficients in silane plasma chemistry. *Contributions to Plasma Physics*, 36(1):3–49, 1996.

[37] William Paul and David A Anderson. Properties of amorphous hydrogenated silicon, with special emphasis on preparation by sputtering. *Solar Energy Materials*, 5(3):229–316, 1981.

[38] Robert A Street. *Hydrogenated amorphous silicon*. Cambridge university press, 2005.

[39] Jeyakumar Ramanujam and Amit Verma. Photovoltaic properties of a-si: H films grown by plasma enhanced chemical vapor deposition: a review. *Materials Express*, 2(3):177–196, 2012.

[40] Di Yan, Andres Cuevas, Yimao Wan, and James Bullock. Silicon nitride/silicon oxide interlayers for solar cell passivating contacts based on pecvd amorphous silicon. *physica status solidi (RRL)–Rapid Research Letters*, 9(11):617–621, 2015.

[41] MK Stodolny, M Lenes, Y Wu, GJM Janssen, IG Romijn, JRM Luchies, and LJ Geerligs. n-type polysilicon passivating contact for industrial bifacial n-type solar cells. *Solar Energy Materials and Solar Cells*, 158:24–28, 2016.

[42] C Malerba, M Valentini, CL Azanza Ricardo, A Rinaldi, E Cappelletto, P Scardi, and A Mittiga. Blistering in cu2znsns4 thin films: correlation with residual stresses. *Materials & Design*, 108:725–735, 2016.

[43] K Takimoto, A Fukuta, Y Yamamoto, N Yoshida, T Itoh, and S Nonomura. Linear thermal expansion coefficients of amorphous and microcrystalline silicon films. *Journal of non-crystalline solids*, 299:314–317, 2002.

[44] C Iliescu, M Avram, B Chen, A Popescu, V Dumitrescu, D Poenar, A Sterian, D Vrtacnik, S Amon, and P Sterian. Residual stress in thin films pecvd depositions. *Journal of Optoelectronics and Advanced Materials*, 13(4):387–394, 2011.

[45] FHM Sanders. On the stress in plasma-deposited a-sic: H films. *Surface and Coatings Technology*, 60(1-3):424–427, 1993.

[46] Mark A Petrich, Karen K Gleason, and Jeffrey A Reimer. Structure and properties of amorphous hydrogenated silicon carbide. *Physical Review B*, 36(18):9722, 1987.

[47] DCH Yu and JA Taylor. Correlation between processing, composition, and mechanical properties of pecvd-sinx, thin films. *MRS Online Proceedings Library*, 188(1):79–84, 1990.

[48] Rui Xu, Kai Yang, Tianqi Zhao, and Li Jiang. Structural evolution and mechanical properties of nitrogen doped hydrogenated amorphous silicon thin films. *AIP Advances*, 10(8):085025, 2020.

[49] GR Wolstenholme, N Jorgensen, P Ashburn, and GR Booker. An investigation of the thermal stability of the interfacial oxide in polycrystalline silicon emitter bipolar transistors by comparing device results with high-resolution electron microscopy observations. *journal of Applied Physics*, 61(1):225–233, 1987.

[50] Frank Feldmann, Massimo Nicolai, Ralph Müller, Christian Reichel, and Martin Hermle. Optical and electrical characterization of poly-si/siox contacts and their implications on solar cell design. *Energy Procedia*, 124:31–37, 2017.